UNIVERSITÉ DU QUÉBEC À MONTRÉAL

PHOTOELECTROCHEMISTRY OF LEAD HALIDE PEROVSKITE

THESIS

PRESENTED
AS PARTIAL REQUIREMENT OF
MASTER OF CHEMISTRY

BY
SALEK ESFAHANI SAMANEH

APRIL 2022

UNIVERSITÉ DU QUÉBEC À MONTRÉAL

PHOTOÉLECTROCHIMIE DE PÉROVSKITE À BASE D'HALOGÉNURES ET DE PLOMB

MÉMOIRE

PRÉSENTÉ
COMME EXIGENCE PARTIELLE
MAÎTRISE EN CHIMIE

PAR
SALEK ESFAHANI SAMANEH

AVRIL 2022

ACKNOWLEDGMENT

I would like to express my special appreciation to Professor. Joshua Byers whose support and knowledge directed me through this research work. Your dedicated guidance provided the encouragement throughout this project. I would also like to thank you for your patience and understanding in any circumstances. Thank you for trusting me, and continuing to have faith in me over the years.

I would like to thank the following people without whom this project would have not been the same. My groupmates Romaric Charles Beugré, Tao Liu ,and Alec Dorval for all the assistance they have provided. Thanks to Nanoqam especially to Gwénaël Chamoulaud and Galyna Shul and all the participants that enabled this research to be possible.

I would like to thank my family and anyone who lives with me or around me that supported me during my studying years. Thanks to my mom for her endless support, to my father in heaven for always believing me and having my back. Thanks to my sister for always being there at difficult times. Thanks to my beloved daughters Sophia and Lia. Thank you for always being such good girls and motivating me everyday in life.

Finally, I thank God for letting me do this through all the difficulties.

DÉDICACE

To Sophia

To Lia

TABLE OF CONTENTS

LIST OF FIGURES

Figure page

LIST OF TABLES

LIST OF ABBREVIATIONS AND ACRONYMES

XRD: X-ray diffraction

SEM: scanning electron microscopy

PL: photoluminescence

EIS: electrochemical impedance spectroscopy

ETM: electron transport materials

HTM: hole transport materials

FTO: fluorine doped tin oxide

UV: ultraviolet

e^-: electron

h+: hole

$E_{(CB)}$: conduction band energy level

$E_{(VB)}$: valence band energy level

MA^+ : methylammonium

FA^+: formamidinium

MAI: methylammonium iodide

$MAPbI_3$: methylammonium lead iodide

$CsPbBr_3$: cesium lead bromide

TiO_2: titanium dioxide

PbI_2: lead iodide

H_2O: water

CO_2: carbon dioxide

CH_4: methane

CH_3OH: methanol

CIGS: copper indium gallium selenide

CdTe: cadmium telluride

DCE: dichloroethane

BQ: benzoquinone

LIST OF SYMBOLES AND UNITS

eV : electron volt

V: voltage (volt)

A: ampere

t: time (second)

µm: micro meter

nm: nano meter

M: molar concentration

S: surface area (m^2)

A : absorbance

°C: degree Celsius

Q: charge (coulomb)

F: Faraday constant (96485.33 C/mol)

Z: oxidation state

i: current density (A/m^2)

ρ: density (kg/m$_3$)

E: potential (volt)

E^0: standard potential (volt)

$E_{int:}$ initial potential (volt)

E_{inv}: inversion potential (volt)

R: gas constant (8.314 J/mol K)

V: applied voltage (volt)

E_{eq}: potential at equilibrium(volt)

η: overvoltage (volt)

i_0: exchange current density (A/cm^2)

α: charge transfer coefficient

F_i: mass flux of species i (mol/s m^2)

C: concentration (mol/m^3)

v : velocity

D: diffusion coefficient (m^2/s)

dC/dx: gradient of concentration

dV/dx :gradient of potential

E_g: bandgap energy (eV)

n_i: intrinsic electron concentration

p_i: intrinsic hole concentration

k : Boltzmann constant ($8.617 x 10^{-5}$ eV/K)

T: absolute temperature (kelvin)]

E_F: fermi energy (eV)

Ec: conduction band energy (eV)

Ev: valence band energy (eV)

Nc: density of states in the conduction band

Ω: ohm

f : frequency (s^{-1})

φ : angular frequency (radian)

Z : impedance (ohm)

j : imaginary number

W: mass (g)

RÉSUMÉ

Les propriétés optoélectroniques exceptionnelles des pérovskites à base d’halogénures de plomb ont donné lieu à de nouvelles études en photocatalyse (qui est basée sur la génération et le transport de charge), notamment dans le domaine de la conversion de l'énergie solaire.

Dans cette recherche, deux types de pérovskites à base d’halogénures de plomb ont été étudiées: l’iodure de plomb méthylammonium ($CH_3NH_3PbI_3$) et une pérovskite inorganique, le bromure de plomb césium ($CsPbBr_3$).

Certaines méthodes telles que le dépôt en phase vapeur et le revêtement par centrifugation sont couramment utilisées pour synthétiser ces matériaux. Dans ce travail, l'électrodéposition du dioxyde de plomb suivie d'une conversion chimique a été utilisée comme méthode de synthèse pour former les pérovskites à base d’halogénures de plomb à température ambiante. En utilisant cette méthode et en ajustant les paramètres électrochimiques, il a été possible de contrôler l'épaisseur et la morphologie du film qui ont un impact direct sur l'efficacité de la pérovskite.

Ensuite, les comportements électrochimique et photoélectrochimique du $CH_3NH_3PbI_3$ ($MAPbI_3$) et du $CsPbBr_3$ ont été étudiés dans du NBu_4PF_6/dichloroéthane. Pour ce faire, la fenêtre de stabilité a été déterminée par l’oxydation et la réduction du film pour les mesures électrochimiques, puis le photocourant a été observé en présence et sans un médiateur redox. Le système photoélectrochimique et les modifications du film à l'interface ont été caractérisés par spectroscopie d'impédance électrochimique (EIS). Il a été constaté que le $MAPbI_3$ présentait un photocourant plus important sous un éclairage en lumière blanche ainsi qu'un taux de corrosion plus élevé. Le $CsPbBr_3$ a plutôt montré une réponse de photocourant plus faible en raison d'une couverture d'électrode moins uniforme et d'une bande interdite plus grande. La spectroscopie d'impédance électrochimique a été utilisée pour quantifier la capacité géométrique, la résistance de recombinaison, la capacité interfaciale et la résistance de transfert de charge des films minces de $MAPbI_3$ et de $CsPbBr_3$ dans une cellule photoélectrochimique.

Les résultats de ce travail permettent de mieux comprendre l'électrodéposition des pérovskites à base d’halogénures de plomb ainsi que leur activité électrochimique et photoélectrochimique.

Mots clés : iodure de plomb méthylammonium, bromure de plomb césium, photoélectrochimie, photocatalyse

ABSTRACT

The outstanding optoelectronic properties of lead halide perovskites have given rise to new studies in chemistry that involve solar energy conversion such as photocatalysis.

In this research, two different lead halide perovskites were studied: the hybrid perovskite methylammonium lead iodide ($CH_3NH_3PbI_3$) and the all-inorganic perovskite cesium lead bromide ($CsPbBr_3$). Preparation methods such as vapor deposition and spin coating are commonly used to make these materials. Here we focus on the electrodeposition of lead dioxide followed by chemical conversion to form lead halide perovskites at room temperature. By using this method and adjusting electrochemical parameters, it was possible to control the thickness and morphology of the film which has a direct impact on the photoactivity of the perovskite. In the subsequent chemical conversion of lead dioxide to a perovskite, several variables were studied including the amount of lead dioxide on the substrate, the concentration of methyl ammonium iodide used and the duration of the chemical conversion process. A systematic variation of these variables enabled the formation of perovskite thin films. The electrochemical and photoelectrochemical behavior of ($MAPbI_3$) and ($CsPbBr_3$) were studied in NBu_4PF_6 / dichloroethane. The electrochemical stability window was determined using linear sweep voltammetry and photocurrent measurements were carried out with and without the presence of a redox mediator. The photoelectrochemical system and the changes to the film at the interface were characterized by electrochemical impedance spectroscopy (EIS). It was found that $MAPbI_3$ showed a larger photocurrent under white light illumination as well as a higher rate of corrosion. $CsPbBr_3$ showed a lower photocurrent response due to less uniform electrode coverage and a larger bandgap. Electrochemical impedance spectroscopy was used to quantify the geometric capacitance, recombination resistance, interfacial capacitance and charge transfer resistance of $MAPbI_3$ and $CsPbBr_3$ thin films in an a photoelectrochemical cell. The results of this work provide a better understanding of the electrodeposition of lead halide perovskites and further insight into their electrochemical and photoelectrochemical activity.

Keywords : methylammonium lead iodide, cesium lead bromide, photoelectrochemistry, photocatalysis.

CHAPTER I

PRINCIPLES AND CONCEPT

This chapter describes the principles of the synthesis and characterization methods used in this research project. It will introduce the main theoretical aspects and techniques necessary to motivate the logic of the applied methods and techniques to realize the research objectives. The theory section is divided into two chapters, with the first chapter discussing solar energy and perovskite materials. Also in this chapter, the synthesis method used in this work, electrodeposition and materials characterization methods including electrochemical methods, XRD and SEM will be discussed. Chapter 2 will focus on photoelectrochemistry and photocatalysis using lead halide perovskite materials as an example.

1.1 Solar energy

One of the most important challenges of today is to find renewable sources of energy to fulfill the energy demand of the growing population and industry. Fossil fuel use increases the level of CO_2 in our atmosphere contributing to the greenhouse effect which results in climate change. Solar energy is an alternative sustainable and abundant source of energy. In fact, numerous photovoltaic technologies are currently available to replace traditional sources of energy, however, there are still major challenges in converting and storing solar energy efficiently and affordably. Some examples of photovoltaic technology include:

1. Crystalline silicon solar cells, which dominate the photovoltaic market. Silicon solar cells are the most used photovoltaic technology in the world, representing about 80% of all solar panel installations(Ranabhat *et al.*, 2016). Silicon solar cells are the most efficient in terms of single-cell photovoltaic devices. Silicon is also the most abundant element on earth and is a great semiconductor for photovoltaic applications with an energy bandgap of 1.1eV(Abdy *et al.*, 2021). However, the difficult multi-process procedure and high cost of making these type of solar cells make their widescale use challenging.

2. Another photovoltaic technology uses thin-film inorganic compounds such as CdTe (cadmium telluride) and CIGS (copper indium gallium selenide) that uses vacuum vapor deposition for film preparation which is energy-consuming.

3. A third generation of photovoltaic technologies are solution-processable thin-film solar cells with moderate power conversion efficiency with low cost of fabrication, like organic photovoltaic cells and dye-sensitized solar cells. Another photovoltaic technology that has drawn a lot of attention recently are perovskite-based solar cells with high power conversion efficiency. The optoelectronic properties of perovskites with their simple and inexpensive film deposition methods make these materials a promising alternative to silicon solar cells. Despite all the progress in perovskite based solar cells, their instability remains a major challenge in their industrial development. Perovskite solar cells have the potential to accelerate the race to find alternative energy generation sources due to a high efficiency combined with simple and low cost fabrication methods.

4. An aspirtational use of solar energy is in photocatalysis that has many advantages for energy generation and storage using solar fuel production like hydrogen evolution by the photocatalytic splitting of water, CO_2 reduction, or degrading organic pollutants. (Dandia *et al.*, 2020; Tonui *et al.*, 2018)

All above-mentioned technologies rely on a semiconductor to convert sunlight to useful energy. Most research focuses on lead halide perovskite photovoltaic devices and the following chapter will summarize the pertinent aspects of this literature with a focus on $MAPbI_3$ and $CsPbBr_3$, which are the lead halide perovskites used this work.

1.1.1 Perovskite

A perovskite is a kind of mineral that first was found in the Ural Mountains as calcium titanate (CaTiO3). It was named after the founder from the Russian Geographical Society (Lev Perovski). In general, a perovskite is any compound that has the same structure as this mineral.

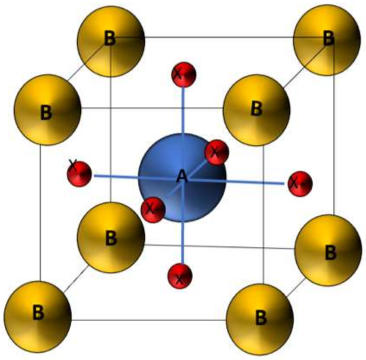

Figure 1.1 Crystal structure of perovskite in form of ABX_3.

The general chemical structure of perovskite follows the formula ABX_3, where A and B are two cations different in size and X is an anion (Figure 1.1). Depending on the atoms or molecules used in the structure, perovskite materials can vary in terms of their properties. For example, in all-inorganic lead halide compounds, cesium could be cation A and lead or tin in the place of cation B and the halides (I, Cl, or Br) occupy the anion site. Lead halide perovskites are popular as they have strong absorption in the visible region, a long charge carrier diffusion length and a tunable bandgap. Another example would be hybrid organic-inorganic lead halide perovskites where the inorganic A site cation is replaced with either methylammonium or formamidinium.

Among these compounds, methylammonium is the most commonly used organic component of the lead halide perovskite structure. However, formamidinium has a favorable energy bandgap of about 1.47 eV (this number is 1.57 eV for methylammonium lead iodide perovskite) (Tonui *et al.*, 2018). The best power conversion efficiencies can be achieved with semiconductors that have a bandgap value between 0.93 eV and 1.61 eV. (Rühle, 2016)

One of the advantages that perovskite photovoltaics have over other solar technologies is that they are able to absorb a broad range of wavelengths of light, converting more sunlight into electricity and providing good efficiency. The other advantage is that perovskites are very simple to produce compared to silicon solar cells that need to be produced at high temperature (over 1000°C) and under vacuum under clean room conditions. However, there remains many challenges in terms of reproductivity and stability of perovskites.

The important factors of perovskites that enable high performance and high efficiency are the following:

1. High optical absorption coefficient.
2. Long carrier diffusion length (defect tolerant nature).
3. Balanced charge transfer.

1.1.2 Halide perovskite

Lead halide perovskites semiconductors are divided into two types of hybrid (organic-inorganic) and all-inorganic halide perovskite. Determining hybrid or inorganic perovskite depends on the A-site ion of ABX_3 structure. The inorganic perovskite contains symmetric and spherical cations in A sites like Cs^+, but organic, asymmetric and polar cations like MA^+ (methylammonium) in hybrid perovskites. In both types, X could be any halide ions of I^-, Br^- or Cl^-.

Inorganic halide perovskites are intrinsically and thermally more stable than their hybrid counterparts because organic MA^+ (methylammonium) and FA^+(formamidinium) cations are more volatile. Hybrid perovskites can be applied in various optoelectronic technologies such as solar cells, photodetectors, light-emitting devices, and also in photocatalysis (Huang *et al.*, 2020; Singh *et al.*, 2020). However, the degradation of these kinds of perovskite motivates ongoing research to find alternative ways to increase their stability.

For example, $MAPbI_3$ degrades under light and oxygen which is caused by the reaction of superoxide (O^{2-}) with the MA^+ cation, while in $CsPbI_3$, Cs^+ are free of acid protons that improve the stability of perovskites to oxygen under illumination. However, some inorganic perovskites are not stable in moisture, heat, light or oxygen. (Zhou et Zhao, 2019)

1.1.2.1 Cesium lead halide perovskites

Hybrid perovskites have higher solar efficiency than inorganic perovskites, but also show lower stability. For example, $MAPbI_3$ degrades easily at temperatures as low as 120 °C. To overcome the challenge of instability, inorganic halide perovskites $CsPbX_3$

(X=Cl^-, Br^-, I^-) have been explored. They are comparable with the hybrid ones in optical properties and their morphology can be controlled during thin film synthesis. Cesium is a suitable inorganic cation as it is also possible to control the bandgap of cesium halide perovskite by the choice of halides. For example the bandgap energy is 1.77 eV for $CsPbI_3$ and 2.38 eV for $CsPbBr_3$. Although a bandgap around 2.3 eV is not ideal for photovoltaic applications, $CsPbBr_3$ still can be a good absorber in perovskite solar cells with reasonable efficiency and has good thermal stability up to 580 °C. Furthermore, a larger bandgap can be useful in photocatalysis where kinetic limitations require a large overvoltage to enable photocatalytic reactions.

1.1.3 Perovskite solar cells

The principles of the semiconductor physics to describe silicon-based solar cells can be used to describe perovskite solar cells. Several studies show that right after photoexcitation in perovskite solar cells, electron-hole pairs are generated, and then they are dissociated into free charges by the electric field generated between the anode and cathode in less than two pico-seconds. The ability of a perovskite solar cell to efficiently convert solar energy into electricity is due to a long charge carrier diffusion length and high carrier mobility (Herz, 2017). Depending on the composition of the perovskite, the electron and hole diffusion length can vary. In some cases, it can reach as high as 1 μm which is large enough for photo-generated charges to reach the charge collecting interfacial layers and electrodes without any recombination.(Tonui *et al.*, 2018)

1.1.4 Perovskite solar cell architectures

Perovskite solar cells consist of a perovskite thin film sandwiched between two electrodes. Interfacial buffer layers can be employed between the active layer and the electrodes to improve charge extraction. There are two types of interfacial layers, one of them is the electron transport material (ETM) and the other one, the hole transport material (HTM). One of the electrodes should be a transparent conducting oxide like fluorine doped tin oxide (FTO).

Two main architectures are found for perovskite solar cells: mesoporous and planar. In the mesoporous structure, the perovskite layers are formed on a porous TiO_2 semiconductor that can create an interpenetrating network between the two phases so that the photogenerated electrons transport thorough the titanium dioxide domain to the cathode while the holes are transported along the perovskite to the anode. Planar solar cells are made using interfacial hole and electron transport materials so that the photo-generated charges created by the perovskite can reach the electrodes. Regardless of the structure, the power conversion efficiency of the device depends on the quality of the perovskite film. In case of low quality perovskite films (poor morphology), the solar absorber film will result in charge accumulation in the bulk that could enhance charge recombination and reduce the performance of the devices.

The efficiency of a solar cell in converting solar energy to useful electricity depends, in part, on the optical absorption of the photoactive material. For example, they need to have an ideal bandgap to absorb the optimal amount of light while maintaining a good open circuit voltage. The ideal bandgap for a semiconductor in solar cells is approximately 1.2 to 1.6 eV to maximize power output. One advantage of perovskite materials are that they have a direct bandgap, which enables the use of thinner materials than silicon, which has an indirect bandgap. (Tonui *et al.*, 2018)

1.2 Electrodeposition

There are many methods available to make perovskites such as vapor deposition or spin coating but precipitation and evaporation can make the variation of morphology of these products difficult to control. For example, using spin coating, the quality of the film decreases when increasing the deposition area. For that reason, devices that are prepared by spin-coating cannot have areas more than a couple of square centimeters. Electrodeposition can be used to make high quality perovskites. Also, the controllable parameters of electrodeposition make it a good method to define and modify the thickness and structure of the perovskite. (Zhang *et al.*, 2015)

Using electrodeposition, it is possible to control the conditions which have a direct impact on the efficiency of perovskites making it possible to modify the optical absorption, morphology, thickness, and conductivity. It can also provide a uniform perovskite film with low grain boundary density that can improve the performance. (Abdy *et al.*, 2021; Popov *et al.*, 2016; SamuScheidtZaiats*, et al.*, 2018) Moreover, electrodeposition is an inexpensive method. Electrodeposition can be used in roll-to-roll processing which can reduce manufacturing costs. (Chen *et al.*, 2015; Jaeyoung Lee a, 2000). For industrial use, where larger area and cost are important, electrodeposition could be an alternative method that is scalable and able to be used for areas of some square meters. In summary, electrodeposition can be used to make films on substrates with complex shapes which can be used in making flexible perovskite solar cells, shows a high deposition rate, and is low cost.

1.1.2 Electrodeposition Fundamentals

In general, electrodeposition is a technology to produce materials by using an applied current or potential in an electrolyte solution to form a thin film or coating. An electrochemical cell is used for electrodeposition and a three electrode setup is often used in a laboratory setting consisting of a working electrode, a counter electrode and a third electrode, which is a reference electrode. By applying current through the electrolyte between the working and counter electrodes, the film can grow on the surface of the working electrode substrate, which in this work is FTO.

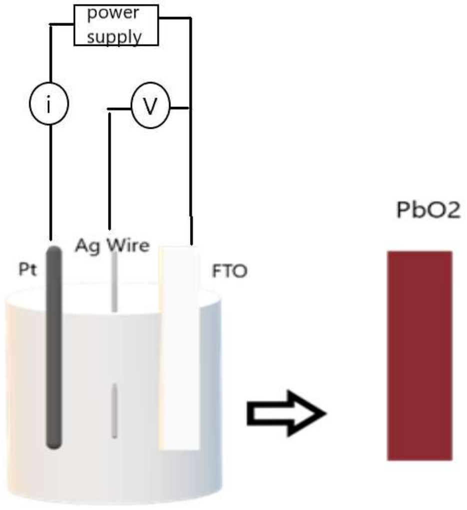

Figure 1.2 Schematic for the electrodeposition of lead dioxide on the surface of a FTO substrate in a three electrode electrochemical cell.

1.2.1.1 Stoichiometry

In the simplest scenario, electrodeposition is an electrochemical process that follows Faraday's law, where the number of moles of material deposited should be proportional to the charge (Q) passed over a defined periotd of time. The mass (W) of the electrodeposited material is related to to the charge by the following equation:

$$W = \frac{A.Q}{z.F} \tag{1.1}$$

Where Q is a total charge flowing through the electrochemical cell, F is Faraday's constant equal to 95.485 C/mol. A is molar mass and z, oxidation state.

We can rewrite this equation as follows:

$$W = \frac{A.I.t}{S.z.F} \tag{1.2}$$

S is the area and i (current density) is equal to I/S, where I is the current.

In this case, it is also possible to calculate the thikness of the film (δ) by the following equation:

$$\delta = \frac{A.i.t}{z.F.\rho} \tag{1.3}$$

Where ρ is the density.

In all of these equations it is assumed that all the current is used for growing the film.

1.2.1.2 Thermodynamics

For the case of metal reduction or oxidation, the equilibrium between metal dissolution from the electrode and the reduction of the metal ion on the surface is measured with respect to a reference electrode:

$$M^{z+} + ze^{-} \leftrightharpoons M \tag{1.4}$$

This equilibrium can change due to the activity of the ionic species following the Nernst equation:

$$E = E^{0} + \left(\frac{RT}{zF}\right) \ln\left[\frac{\alpha_{ox}}{\alpha_{red}}\right] \tag{1.5}$$

E^0 is the standard redox potential and R is the gas constant (8.314 J/mol K), T is absolute temperature, α_{ox} and α_{red} are the activity of oxidized and reduced species.

Also considering the approximation of the concentration of the ionic species instead of activity in solution with the concentration lower than 10^{-3} mol/L, we can relate it to the concentration of our metal by the following equation:

$$E = E^{0} + \left(\frac{RT}{zF}\right) \ln[M^{z+}] \tag{1.6}$$

A Pourbaix diagram (potential vs pH, Figure 1.3) also can be used to determine which species is more stable for a given electrode potential and pH.

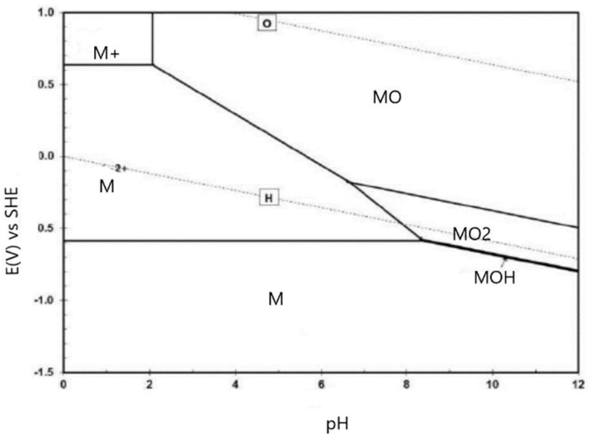

Figure 1.3 Pourbaix diagram for a type of metal M.

1.2.1.3 Kinetics

When an external potential is applied to the system, the metal ion is reduced on the surface of our substrate (electrode) or the metal is oxidized to a metal ion (depending on the applied potential and electrolyte).

By applying an external potential, the Faradaic current leads to an electrochemical transformation which depends to the overpotential. In this situation, we can relate the electron transfer rate to the overvoltage η by the Butler-Volmer equation where:

$$\eta = V - E_{\text{eq}} \tag{1.7}$$

V is the applied voltage and E_{eq} is the potential at equilibrium.

$$i = i_0[\exp(-z\alpha f\eta) - \exp(z(1-\alpha)f\eta)] \tag{1.8}$$

i is the current density, i_0 the exchange current density, α is charge transfer coefficient and $f=F/RT$ (Zangari, 2018).

For example, for a cathodic electrodeposition, a negative overpotential results in metal reduction and electrodeposition. In this case, the metal ions diffuse to the electrode (it may have chemical or structural transformation) and can be reduced at the electrode which makes the electrodeposition of the film possible.

1.2.2 Galvanostatic electrodeposition

Galvanostatic electrodeposition is an electrodeposition technique that uses a constant current during the formation and growth of a thin film. The electrochemical growth of the film takes place in a two or three electrode electrochemical system . The electrolyte contains the metal-containing salts in a solvent. In galvanostatic electrodeposition, current density can affect the process of film growth, coating morphology and the deposition reaction rate. (Gamburg et Zangari, 2011)

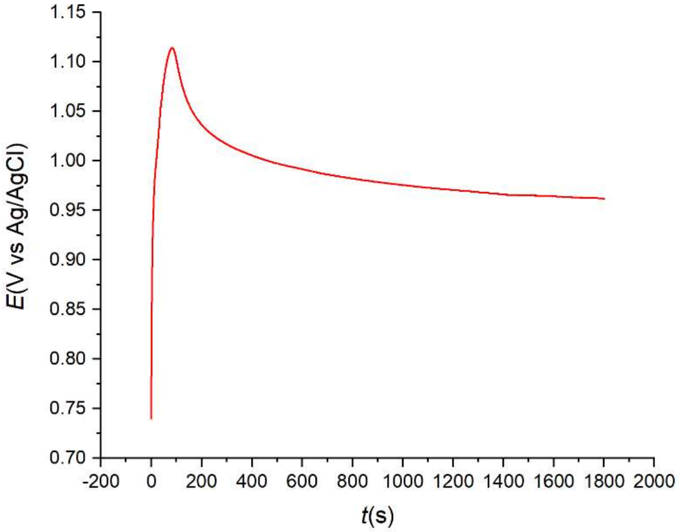

Figure 1.4 Galvanostatic curve of the lead dioxide electrodeposition.

Figure 1.4 shows the potential/time curve of the galvanostatic electrodeposition of PbO_2 on FTO , at the beginning of the process, the electrode potential increases from 0.75 to 1.12 (V vs Ag/AgCl) wich is the start of growth activation, then it gradually decrease to 0.97 (V vs Ag/AgCl) and remains constant, while the amont of PbO_2 deposited on the electrode increases with time at this constant potential.

1.2.3 Electrode/Electrolyte Interface

When an electrode comes in contact with an electrolyte, charge distribution at the interface occurs that could be modeled as a capacitance at the interface. As we can see in Figure 1.5, the distribution of ions at the interface is balanced including ions at the inner (IHP) and outer Helmholtz (OHP) layer and also in the diffuse layer, which is the result of the interaction between thermal motion and electrostatic interaction. The thickness of double layer *L* depends on the ion concentration. At higher concentration, *L* is smaller and at lower concentration, *L* is larger. The behavior of the interface between the electrode and electrolyte is described as a model of two capacitors in series which is a function of ion concentration and applied potential. The interface of the electrode-electrolyte will be discussed in further detail in the next chapter in the photoelectrochemistry section.

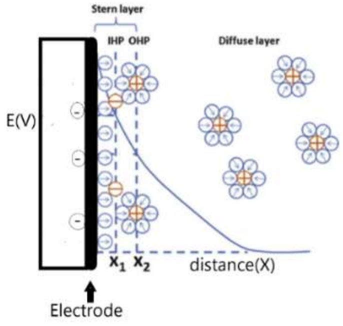

Figure 1.5 Distribution of charge at the interface of electrode and electrolyte, adapted from (Zangari, 2018).

1.3 XRD (X-Ray Diffraction)

The crystallinity and structure of a perovskite film can be determined using XRD. By this method, it is also possible to measure the orientation and size of the grains. XRD is a complimentary non-destructive method to other techniques of characterization that can be used for phase identification, crystal orientation, crystallite size, and structure.

XRD peaks are produced by constructive interference of a monochromatic beam of X-rays that can be scattered at specific angles from each set of lattice planes in a sample. From the atomic positions within the lattice planes, the intensity of the peaks can be determined. Moreover, using XRD, it is possible to observe how the perovskite thin film's internal structure changes over time due to air and moisture exposure. For example, in the XRD of $MAPbI_3$ that is exposed to air and humidity, a peak of PbI_2 becomes more intense which is due to the degradation of the $MAPbI_3$ perovskite. (Holder et Schaak, 2019)

1.4 Scanning Electron Microscope (SEM)

An electron microscope has a higher spatial resolution than an optical microscope with the difference due to the source illumination. The source of an optical microscope is visible light while the source of an electron microscope is an accelerated electron beam. Electrons have a shorter wavelength compared to visible light and can image very small particles from some micrometers to some nanometers (some electron scanning microscopes have a resolution up to 1nm and they can magnify up to 300,000 times).

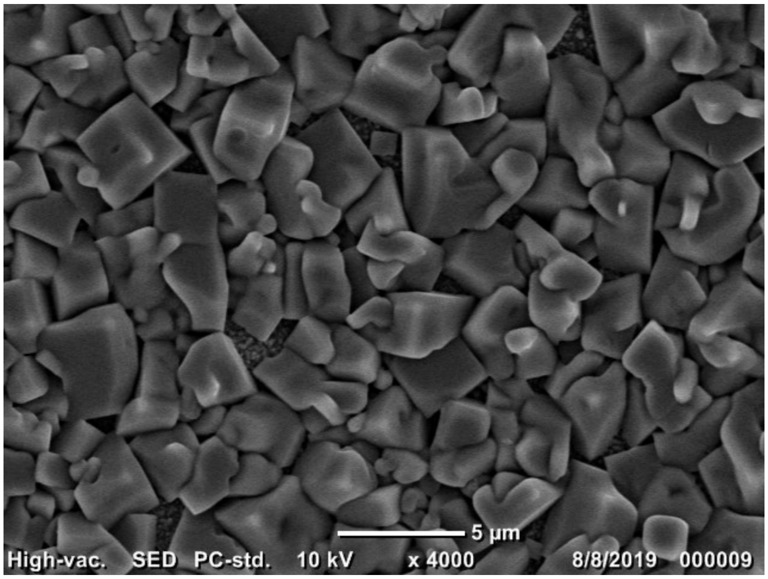

Figure 1.6 SEM image of methyl ammonium lead iodide on FTO

In this work, scanning electron microscopy (SEM), was used to observe the morphology of perovskite films as well as asses their surface coverage as a function of synthesis conditions (Figure 1.6).

1.5 Cyclic voltammetry

Cyclic voltammetry (CV) is an electrochemical technique that is commonly used to measure the current as a function of electrode potential to explore the reduction and oxidation processes of redox active species. Measurement of current as a function of the applied potential between the working and reference electrode provides information on the characteristics of the electrochemical reaction. During a cyclic voltammetry measurement, the potential varies linearly as a function of time (t) over an interval between the initial potential (E_{int}) and an inversion potential (E_{inv}). The first cycle ends when the potential returns to the initial point E_{int}. The variation of the potential is carried out at a certain rate which is called scan rate (v) in (V/s). The potential of the working electrode at a specific time V(t) is given by the following relation :

$$V_t = E_0 \pm \nu t \tag{1.9}$$

The current is measured over the same potential interval. Figure 1.7 is the cyclic voltammogram of an electrochemical system containing a redox couple. The sweep of potential generates a redox reaction. An anodic reaction (oxidation) is occurring when scanning from E_{int} to E_{inv}.

$$Red \rightarrow Ox + n\,e^{-} \tag{1.10}$$

And a cathodic reaction (reduction) illustrated by the reduction peak during reverse scanning from E_{inv} to E_{int}.

$$Ox + n\,e^{-} \rightarrow Red \tag{1.11}$$

The drop of current following the oxidation or reduction current peak is due to a decrease in the concentration of electroactive species near the electrode surface, where the current becomes controlled by diffusion at the electrode/solution interface. The non-zero currents observed at the potentials $\mathrm{E_{int}}$ and $\mathrm{E_{inv}}$ correspond to capacitive cathodic and anodic currents which depend on the electrochemical active surface area.

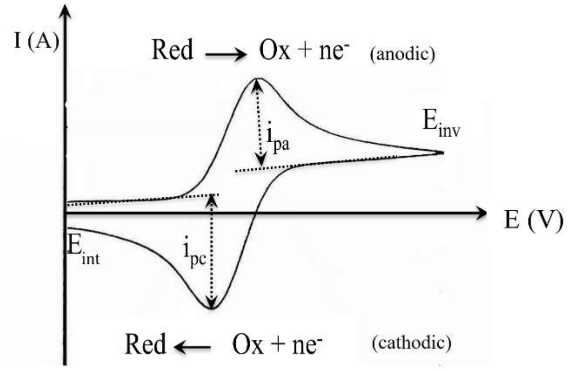

Figure 1.7 Cyclic voltammetry curve which shows the generated current related to potential sweep between E_{int} and E_{inv}.

In voltammetry, the Nernst equation (1.12) relates the potential E to the standard potential of a species (E_0) and the activities of reduced analyte (red) and oxidized (Ox) in an electrochemical cell at the equilibrium.

$$E = E^0 + \frac{RT}{nF} \ln \frac{(Ox)}{(Red)} \tag{1.12}$$

Where F is Faraday's constant, R is the gas constant, n is the number of electrons exchanged, and T is the temperature.(Elgrishi *et al.*, 2018)

1.6 Electrochemistry Impedance Spectroscopy

Electrochemical impedance spectroscopy (EIS) is a method that is used to measure the impedance of electrode reactions such as charge transfer, diffusion or the changes in electrode interface. The equivalent resistance and capacitance values can be used for the evaluation of the electrochemical double layer structure and charge transfer parameters. EIS is a non-destructive method for the characterization for both faradaic processes like charge transfer during redox reaction and resistance of the electrolytic medium between the working and reference electrode. (Itagaki *et al.*, 2007)

This technique involves applying a constant potential to the working electrode, on which a sinusoidal voltage E_{we} is superimposed at various frequencies, *f,* and at low amplitude V_{a}

$$E_{we} = V_a sin(\omega t) \tag{1.13}$$

Which leads to a sinusoidal current I_{we} with amplitude I_{a} and a phase angle φ.

$$I_{we} = I_a \sin\left(\omega t + \varphi\right) \tag{1.14}$$

E_{we} and V_{a} are in volts (V), I_{we} and I_{a} in ampere (A), φ is the angular frequency in radian ($\omega= 2\pi f$, where f is the frequency in s^{-1}), t is the time in seconds.

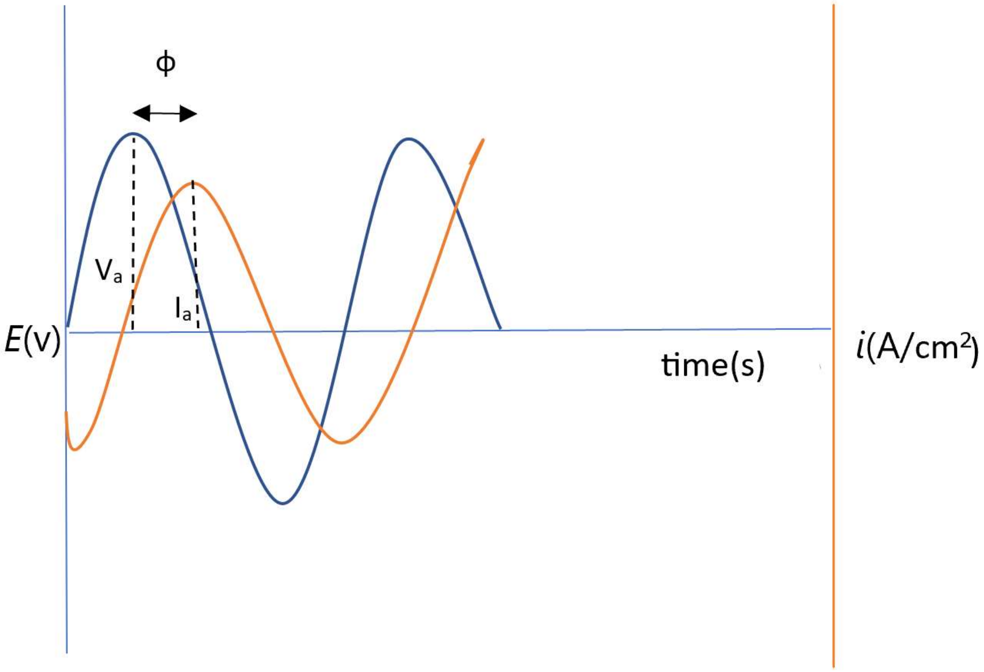

Figure 1.8 Electrochemical response (I_{a} with the angle φ) after imposing a sinusoidal voltage E_{we}.

The resulting relationship between voltage and current as a function of frequency allows interpretation of the faradic and non-faradic processes taking place at the electrode/electrolytic interface. The Z_{we} impedance of the system is defined as a function of E_{we} and I_{we} corresponding to Ohm's law.

$$Z_{we} = \frac{E_{we}}{I_{we}} = Z_0 \frac{sin(\omega t)}{\sin(\omega t+\varphi)} = Z_0(cos(\varphi) + \sin(\varphi)) \tag{1.15}$$

$$Z_{we} = Z_{re} + jZ_{im} \tag{1.16}$$

Where Z_{we} is in (Ohm), φ is phase shift in (rad), j is imaginary number ($j^2 = -1$), Z_{re} is real part of impedance and Z_{im} is the imaginary part.(Itagaki *et al.*, 2007)

Impedance is a more complex concept than resistance, where the input and output signals are always in phase and do not depend on the frequency. On the other hand, the impedance values depend on the frequency. In this technique, impedance is measured as a function of frequency. In order to better interpret the impedance values under different conditions, the models that can represent electrical circuits equivalent to the electrochemical systems are essential. In a Nyquist diagram we can see the imaginary part of the impedance ($-Z_{im}$), which represents the capacitive component of the circuit along with its real part (Z_{re}) which represents its resistive component (Figure 1.9). Every point on this diagram corresponds to a different frequency, with the high frequencies being at the lowest values of Z_{re}. Figure 1.9 is only used here to explain some concepts related to impedance measurements. In this figure, the intersection of the curve at the high frequency defines the resistance in series R_S, while at low frequencies, the intersection of the curve corresponds to (R_S + R_{ct}), which makes it possible to obtain the resistance of charge transfer R_{ct}.

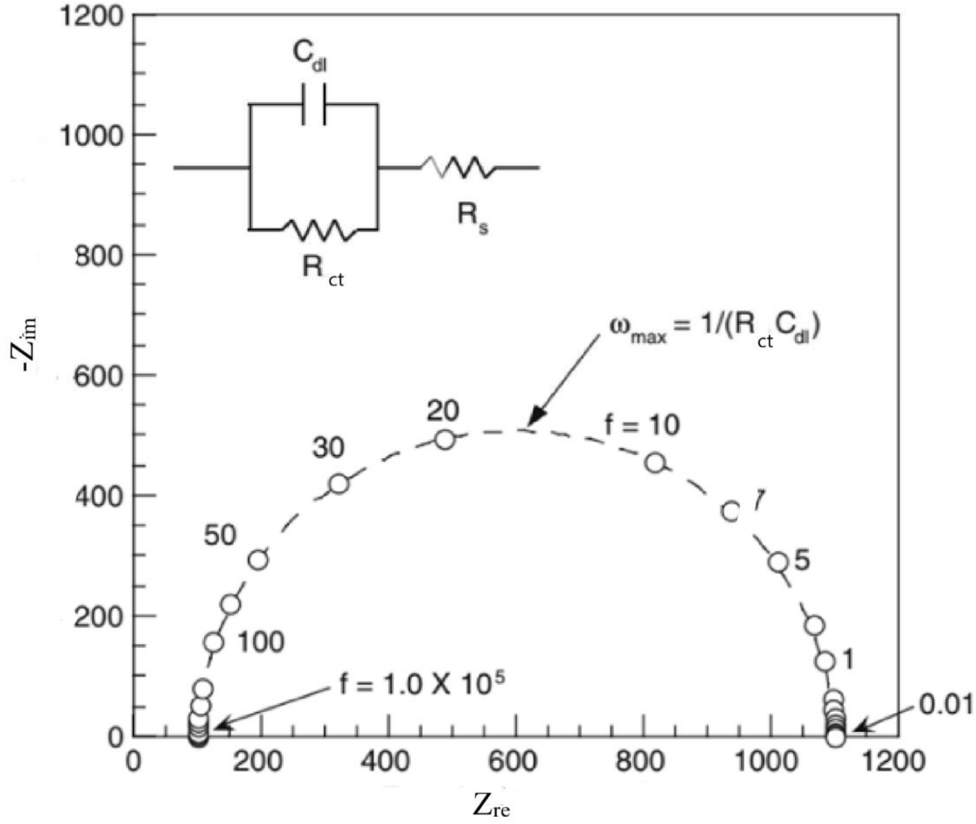

Figure 1.9 A model Nyquist diagram (both $-Z_{im}$ and Z_{re} are in ohm).

.

Electrochemical impedance spectroscopy is a very useful technique to investigate the processes that take place at the interface of semiconductor materials (Klotz *et al.*, 2019). In this work, it was used to monitor changes occurring at the interface of $MAPbI_3$ and $CsPbBr_3$ during electrochemical measurements as a function of electrode potential and electrolyte composition. Also the technique was used to study changes at the interface under illumination.

CHAPTER II

PEROVSKITE PHOTOCATALYSIS

This chapter is about the photocatalytic activity of lead halide perovskites. The first section focuses on the principles of photoelectrochemisty followed by an introduction to photocatalysis and the use of perovskites in this field of research.

2.1 Photoelectrochemical systems

Photoelectrochemistry uses a semiconductor electrode material to absorb light to create free charge carriers that can be used for electrochemical reactions at the electrode/electrolyte interface. Introducing nanostructured semiconductors for light-driven water splitting opened a new opportunity for semiconductor photoelechtrochemistry and photocatalysis. (Peter, 2016)

By illuminating a semiconductor with photons that have higher energy than the bandgap energy, an electron-hole pair is created. If this pair can be separated, electrons can flow to an acceptor species, or an electron comes to fill the hole, consequently, the light energy can be stored for a very short time. As this time is too short, the electron-hole pair can recombine easily. Thus, for creating energy from incident light, it is necessary to find a way to separate the electron and the hole before recombination, for example by controlling the potential. If the electron or hole can be engaged in a redox reaction then they can be separated before reacting.

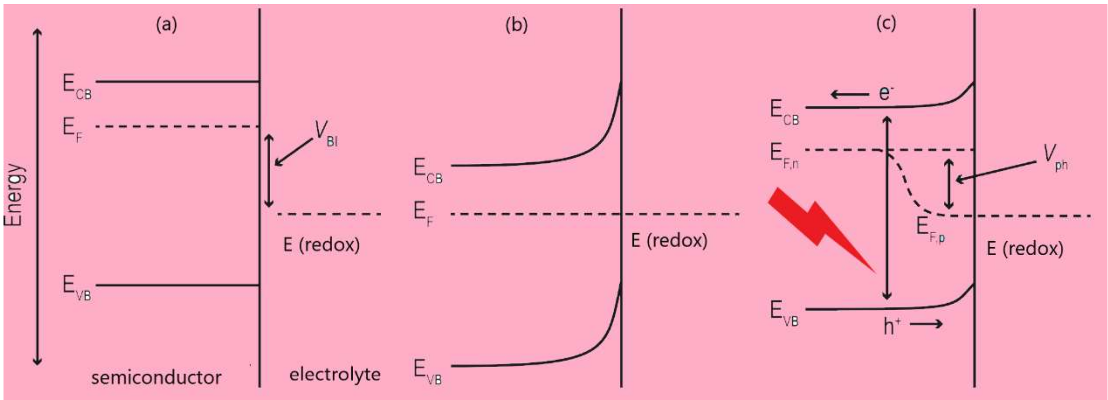

Figure 2.1 The semiconductor/electrolyte junction for an n-type semiconductor (a) before equilibrium, V_{BI} is the difference of fermi level and electrolyte energy. (b) equilibrium at dark. (c) under illumination and generation of electron-hole pair. adapted from (Mayer, 2017)

When a semiconductor is immersed in an electrolyte, charge transfer happens at the interface due to the difference in electrochemical potential of the two phases. The result is the development of electrical field at the surface of the semiconductor/electrolyte interface. For example, in an n-type semiconductor, by the formation of an electron-hole pair in the space charge region (we will talk about this region more detail in the coming section of 2.1.4) by illumination, the electron goes to the bulk of the semiconductor and the hole goes to the surface, so the electric field at the interface can separate the electron and hole (the electric field is represented by band bending in the semiconductor). If a redox agent exists in the electrolyte with suitable redox potential, the electron-hole transfer can happen providing photoelectrochemical activity through light activation. (Bard, 1980; Peter, 2016)

In the following sections, the behavior of the semiconductor/electrolyte surface under different conditions is discussed.

2.1.1 Semiconductor physics

The semiconductor has a key role in the photoelectrochemical process. The semiconductor absorbs photon energy and the interface between the semiconductor and the liquid is responsible for the subsequent (electro)chemical steps and energy conversion.

As already mentioned, there are two different types of charge carriers in a semiconductor which are electrons and holes. By photoexcitation, an electron from the valence band goes to the conduction band and so leaves a hole behind in the valence band.

To determine the conductivity of a semiconductor it is necessary to know the concentration of both electrons and holes. The conductivity in an intrinsic semiconductor is controlled by the bandgap. From the Boltzman equation:

$$n_i p_i = \text{constant}\,\exp\left(\frac{-Eg}{kT}\right) \tag{2.1}$$

n_i is intrinsic electron concentration, p_i is intrinsic hole concentration, k is Boltzmann constant and T is absolute temperature.

In order to improve the conductivity in semiconductors, dopants are introduced into the material by introducing a specific impurity into the host lattice. When a semiconductor is doped with donors, it is called an n-type semiconductor and for a semiconductor that is doped with electron acceptors, is called a p-type semiconductor. In n-type semiconductors, electrons are the majority carriers while in p-type semiconductors, holes are the majority carrier.

The conductivity of a semiconductor depends on the free carrier concentrations by the following equation:

$$\sigma = qn\mu_n + qp\mu_p \tag{2.2}$$

This equation shows that the electrical conductivity (σ) relates to the charge (q) and its concentration in the semiconductor as well as charge carrier mobility (μ), as we have mobility for both electrons and holes so the conductivity depends on the sum of electron and hole mobilities. By doping a semiconductor, it is possible to control the conductivity for photoelectrochemical experiments. (Tan *et al.*, 1994)

An energy level diagram for an n-type semiconductor is shown in Figure 2.2. One important quantity in this figure is Fermi energy that is a measurement of the free energy of electrons.

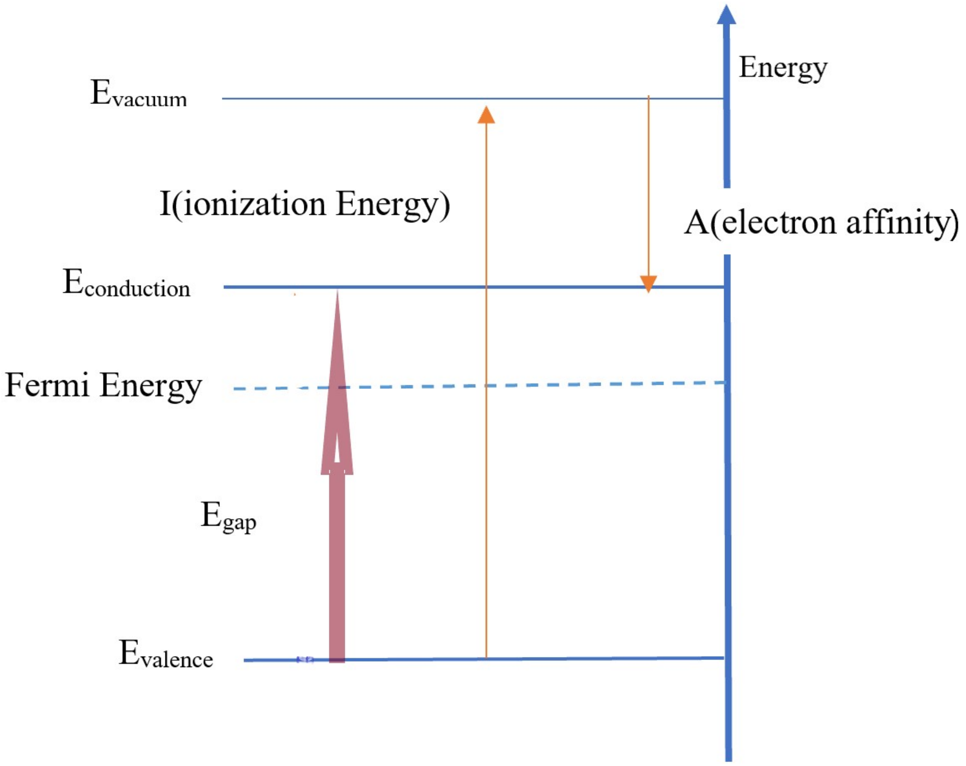

Figure 2.2 Energy diagram for n-type semiconductor. Adapted from (Peter, 2016).

This diagram is related to n-type semiconductor which is doped by electron donor, E_{vaccum} is the vaccum energy level, E_{gap} is band gap energy, $E_{\text{conduction}}$ is conduction band edge energy and E_{valence} is valence band edge energy. In an n-type semiconductor, E_f(fermi energy level) is closer to the conduction band and in p-type that is doped by electron acceptor and creats holes, the Fermi level is closer to the valence band.

When an n-type semiconductor is doped with electron donor species, the crystal lattice of donor atoms can be ionized at room temperature to release electrons into vacant levels in the conduction band. The concentration of electrons that has moved from the valence band to the conduction band under conditions of thermal equilibrium can be measured by the Fermi–Dirac equation:

$$n = Nc \left[\frac{1}{1+e^{\left(\frac{Ec-Ef}{K_B T}\right)}} \right] \tag{2.3}$$

Ec is conduction band energy (eV), Ef is fermi energy (eV), and Nc is the density of states in the conduction band. In normal doping, the exponential is much larger than one, so we can rewrite the equation as follows (Boltzmann equation):

$$n = Nc\ exp - \left(\frac{Ec-Ef}{K_B T}\right) \tag{2.4}$$

In p-type doping, electron acceptors can accept electrons from the valence band, so they create holes. the concentration of holes under thermal equilibrium can be measured by the following equation:

$$P = Nv\ exp - \left(\frac{Ev-Ef}{K_B T}\right) \tag{2.5}$$

N_V is the density of states in the valence band.

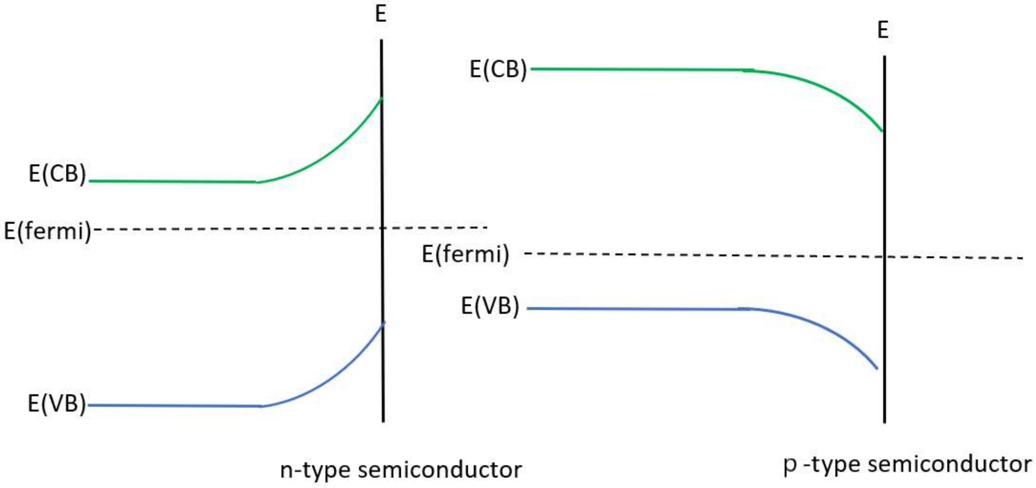

Figure 2.3 Energy band bending diagrams of n-type and p-type semiconductor under depletion conditions.

The Fermi level in a p-type semiconductors is close to the valence band while in a n-type semiconductor, it is near the conduction band as shown in Figure 2.3.

In general the concentration of holes n_p is given by:

$$n_p = n_i^2 = N_C N_v \exp - \left(\frac{E_{gap}}{k_B T}\right) \tag{2.6}$$

n_i is the intrinsic electron density

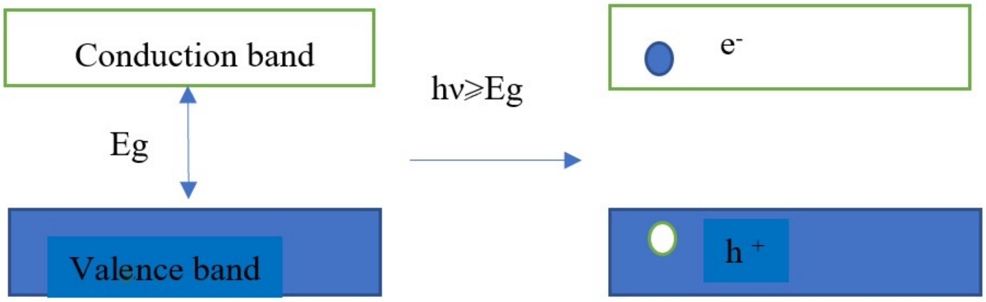

Figure 2.4 Creation of an electron-hole pair by absorption of a photon that is greater in energy than the bandgap energy of a semiconductor.

2.1.2 Semiconductor/electrolyte junction

The semiconductor/electrolyte interface can be described by considering the example of an n-type semiconductor (for a p-type, sign of the charge and band bending are reversed) in contact with electrolyte in dark and without any redox system. If there is no electron transfer at the interface, then the electrode behaves as a capacitor. We can introduce a flat-band potential as the potential where there is no excess charge on the electrode and by consequence no electric field. Therefore, when applying a potential more positive than the flat-band potential, electrons are removed from the electrode, which result in a depletion condition with a positive space charge region due to the ionized donor atoms. This positive space charge region creates an electric field that depends on the distance from the surface and the variation changes the energy of electrons and holes as reflected by the band bending as shown in Figure 2.3. The positive charge of the semiconductor is balanced by the ions of the electrolyte. The majority of the potential drop is in the space charge region.

2.1.3 Semiconductor/redox electrolyte

If a semiconductor is in contact with a redox couple, electron transfer occurs across the interface. In the example of an n-type semiconductor, if the redox Fermi level is lower in energy than the Fermi level in the semiconductor, electrons are transferred to a redox species until an equilibrium is reached. This transfer of charge results in the formation of a depletion region which is shown in Figure 2.5. The magnitude of the band bending is equal to the difference between the Fermi level of the semiconductor and the redox electrolyte.

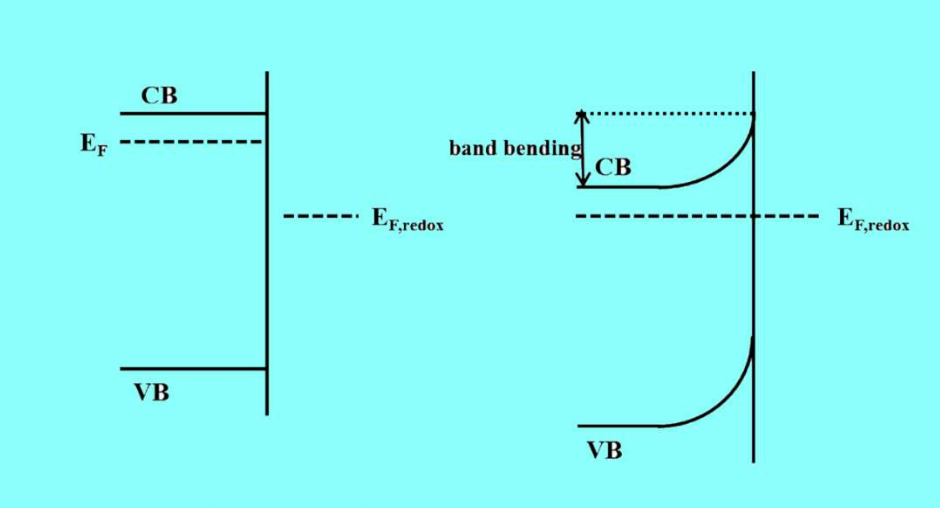

Figure 2.5 Formation of a space charge region and band-bending in an n-type semiconductor. Adapted from (Peter, 2016).

2.1.4 The semiconductor/electrolyte junction under illumination

As discussed in section 2.1.3 when a photon with an energy greater than the energy of the bandgap strikes a semiconductor, electrons become excited from the valence band to the conduction band creating electron-hole pairs. As shown in Figure 2.6, at the interface between the semiconductor and electrolyte with a redox couple, the bands are bent. Under illumination, the photogenerated holes can accept electrons from the electron donor of the redox couple. In an n-type semiconductor, the concentration of holes in the dark is much lower than the electrons and the photogenerated hole is a minority carrier. Although oxidation in the dark does not occur, it becomes possible following illumination as holes are generated.

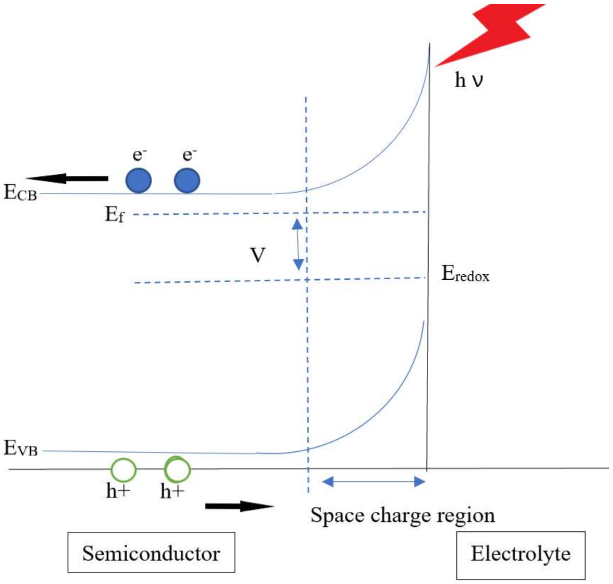

Figure 2.6 Interface of semiconductor in electrolyte in presence of redox agent under illumination.

The life-time of the minority charge carrier determines the efficiency of the photo-catalysis reaction. In an n-type semiconductor, the concentration of electrons is determined by the doping density and can be transported only by diffusion (diffusion length) before recombination due to the lack of an electric field in the bulk of the material. Therefore, the probability of separation of the electron-hole pair is much higher in the space charge region. If the minority carriers reach the space charge region then the electron-hole separation efficiency can be increased. If charge transfer at the semiconductor-electryolyte is not rapid enough, minority carriers will build up in the space charge region causing the band bending to change and increasing charge carrier recombination. (Mayer, 2017; Peter, 2016)

2.2 Photocatalysis

As previously mentioned in the first chapter, solar energy is one of the alternative sources of energy that is vast and durable and photocatalysis is a way to transform sunlight into energy that can be stored. There are three different methods to use solar energy and generate power including photothermal, photovoltaic and photocatalysis. With photocatalytic processes, we are also able to transform abundant molecules like H_2O into H_2 by water splitting or CO_2 into CH_4 or CH_3OH by CO_2 reduction. (Kumar, A. *et al.*, 2020)

Photocatalysis has always been an interesting subject for solar energy conversion and it is also an important method for the degradation of organic waste in water. In a photocatalytic transformation, electron-hole pairs generated by photoexcitation are transferred to a reactant in solution to initiate a degradation reaction. In a photocatalytic reaction, light with the appropriate energy which is equal to or greater than the bandgap energy (Eg) arrives at the surface of semiconductor materials, electrons (e^-) get excited from the valence band (VB) to the conduction band (CB) that leaves holes (h^+) behind so that they can get participate in the redox reaction. The generated holes and electrons can be used in many different reactions such as the degradation of an organic pollutant or CO_2 reduction, hydrogen production or water-splitting reaction. (Dandia *et al.*, 2020; Kumar, A. *et al.*, 2020; Wang, K. *et al.*, 2020)

To illustrate the complexity of a photocatalytic reaction, an example of photooxidation is considered. Through illumination of a semiconductor photocatalyst, a photon with sufficient energy can promote one electron (e^-) from the valence band (VB) that goes to the conduction band (CB), with a hole (h^+) being created in the (VB) where the hole is the oxidizing agent and the electron is the reducing agent. This photooxidation process can be described by the following steps for a photodegradation of organics: (Chong *et al.*, 2010; Wang, W. *et al.*, 2015)

photocatalyst + $h\nu \rightarrow e^- + h^+$ (1)

Photoexcited scavenging: $(O_2)_{ads} + e^- \rightarrow O_2^{\bullet -}$ (2)

Oxidation of hydroxyls: $OH^- + h^+ \rightarrow OH^\bullet$ (3)

Photodegradation of organic by $OH^\bullet$: organic + $OH^\bullet \rightarrow CO_2 + H_2O$ (4)

Direct photoholes: organic + $h^+ \rightarrow$ Intermediates/$CO_2 + H_2O$ (5)

Protonation of superoxides: $O_2^{\bullet -} + OH^\bullet \rightarrow HOO^\bullet$ (6)

Co-scavenging of e: $HOO + e^- \rightarrow HO_2^-$ (7)

Formation of H_2O_2: $HO_2^- + H^+ \rightarrow H_2O_2$ (8)

It is also possible that charge carriers are lost by trapping (TR) and recombination (RC):

Charge carrier trapping of electron: $e_{CB} \rightarrow e_{TR}$ (9)

Charge-carrier trapping of hole : $h_{VB} \rightarrow h_{TR}$ (10)

The photoexcited electron recombines with the VB hole in nanoseconds and generates heat.

Electron–hole recombination: $e_{TR} + h_{VB}(h_{TR}) \rightarrow e_{CB}$ + heat (11)

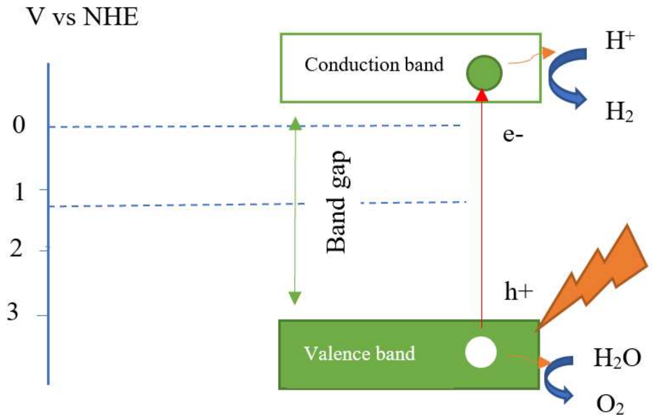

Figure 2.7 Photocatalytic activity of a semiconductor.

Semiconductor-assisted photocatalysis is a useful approach for using light to drive chemical transformations. For optimal photoresponse with sufficient energy to induce oxidation and reduction reactions, the choice of semiconductor with appropriate bandgap is important. Some semiconductors have already been used for photocatalysis like TiO_2, CdS ou ZnO. Nowadays, the application of lead halide perovskites as a photocatalyst is being considered, due to their simple preparation and the ability to tune their bandgap by varying their composition. However, there are still some challenges in working with them as they are unstable in polar solvents and they can easily be degraded. (Wang, W. *et al.*, 2015)

2.2.1 Photocatalytic activity of perovskites

In the first chapter, the structure of perovskite materials which follows the formula of ABX_3 were presented. Several elements can be replaced at A, B and X sites where their variation leads to different materials with different photocatalytic activities. An ideal perovskite has cubic symmetry where the A-cations are at the center of the cube and the B-cations are coordinated with 6 anions in an octahedral model. They can also have different symmetries of orthogonal, tetragonal, monoclinic, rhombohedral, and triclinic structures. These different structures can affect the electronic structure that influences the photocatalytic properties. For example, replacing or doping of cations at both A and B sites with different elements can change the composition and symmetry that can result in changes in structure and light absorption, which affects the photocatalytic activity of the perovskite materials.

As already mentioned in the previous section, reactions that are involved with photocatalytic materials usually follow these three steps:

Absorption of photons to generate electron-hole pairs, charge separation and migration to reaction sites on the photocatalyst surface, and then the chemical redox reaction at the surface by the photogenerated holes and electrons. Therefore, a desirable photocatalytic material should represent strong light absorption, efficient charge separation and the appropriate redox ability for the required reactions. For these reasons, halide perovskites can be an ideal choice due to their optoelectronic properties being tunable and having a direct bandgap, long carrier diffusion lengths, and high carrier mobility. Compared to many other semiconductor catalytic materials, perovskites are easy to prepare. All-inorganic halide perovskites like $CsPbX_3$ (X: halide) have been used for photocatalytic reactions, especially the $CsPbBr_3$ perovskite. By changing the halide or having mixed halide compositions with different ratios, the photocatalytic activity can be modified. The narrow photoluminescence with high quantum yield makes these materials good potential candidates for photovoltaic applications and light emission. The excellent quantum yield of photoluminescence is clear evidence of the significant reduction of non-radiative recombination pathways. Thus, after photoexcitation, a pool of photoexcited carriers are available that can be used in different ways such as in solar cells or photocatalytic processes. The physico-chemical properties of perovskite materials make these materials very well-known for their photovoltaic applications. They could also be highly efficient photocatalysts taking advantage of these properties and use photo-induced electrons-holes to drive redox reactions. (Cardenas-Morcoso *et al.*, 2019; Huang *et al.*, 2020; Kumar, S. *et al.*, 2020)

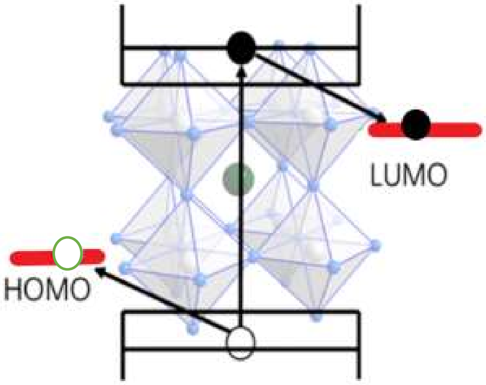

Figure 2.8 Creation of electron-hole pair in perovskite. Adapted from (Wang, K. *et al.*, 2020).

CHAPTER III

EXPERIMENTAL

3.1 Perovskite synthesis and electrode preparation

Materials: Fluorine doped tin oxide coated glass side (FTO, Sigma-Aldrich), sodium acetate 99%(CH_3COONa, Sigma-Aldrich), lead acetate trihydrate ($Pb(CH_3CO_2)_2.3H_2O$, Sigma-Aldrich), methylammonium iodide 98% (CH3NH3. I, Sigma-Aldrich), cesium bromide 99.9% (CsBr, Sigma-Aldrich), hydrobromic acid 48%(HBr, Sigma-Aldrich were used as received and without further treatment or purification. High-purity solvents and deionized water (18.2 MΩ cm) were used for preparing the electrodeposition and chemical conversion solutions.

Before electrodepositiom, FTO substrates were rinsed with acetone, methanol and nanopure water (each one for 20 minutes in an ultrasonic bath). They were dried by N_2 followed by one hour of drying in the oven with 100ºC. Electrodeposition was carried out in a three electrode electrochemical cell using FTO, Ag wire and Pt mesh cylinder as working electrode, reference electrode and counter electrode respectively. An aqueous solution of lead(II) acetate trihydrate (0.1 M) and sodium acetate (1.0 M) was used for the electrodeposition of PbO_2. After dissolving sodium acetate, the pH was adjusted to 5.8 and then adjusted to 5.5 after adding lead(II) acetate trihydrate using concentrated acetic acid. The electrodeposition was performed at ambient temperature in air. The surface area of the working electrode was (1.0 × 2 cm^2) and the current density was kept constant at 0.25 mA/cm^2 for different elecctrodeposition times (100s to 900s). Following the electrodeposition of the PbO_2 film, the electrode was rinsed three times with nanopure water. Galvanostatic electrodeposition of PbO_2 proceeds by the following reaction:

$$Pb^{2+}(aq) + 2H_2O(l) \rightarrow PbO_2(s) + 4H^{+}(aq) + 2e^{-} \tag{3.1}$$

$CH_3NH_3PbI_3$ synthesis: Methylammonium lead iodide ($CH_3NH_3PbI_3$) was synthesized using a one step chemical conversion by immersing the PbO_2 film in a solution of methylammonium iodide in iso-propanol at different concentrations (0.04, 0.05, 0.1, and 0.2 M) for either 30 or 60 minutes at room temperature. Films were dried by annealing for 10 minutes at 100ºC in an oven under ambient conditions. The open circuit potential was monitored during chemical conversion using a potentiostat.

$CsPbBr_3$ synthesis: The cesium lead bromide was synthesized using a two step chemical conversion. In the first step, the PbO_2 film was immersed in HBr (0.05M) in ethanol for two hours for chemical conversion to $PbBr_2$ (color changed completely from brown to white) followed by chemical conversion to $CsPbBr_3$ by immersing the $PbBr_2$ film into a solution of CsBr (0.02 M) in methanol for three hours. The obtained $CsPbBr_3$ film was annealed at 100ºC for 10 minutes.

3.2 Characterization

The crystalline pahase of the perovskite films was determined using an X-Ray diffractometer (Bruker - D8 Advance, Cu Kα (1.5418 Å) radiation). UV-Visible spectra were collected using a UV-Visible spectrometer (Perkin Elmer, Lambda 750), and the morphology of the films was studied using a scanning electron microscope (JEOL

JSM7600F). Profilometery (Bruker Dektak XTL) was used to measure the thickness of lead iodide film on FTO.

3.3 Electrochemistry and photoelectrochemistry

Materials: Tetrabutylammonium hexafluorophosphate 99% ($(CH_3CH_2CH_2CH_2)_4N(PF_6)$, Sigma-Aldrich), p-benzoquinone 98% ($C_6H_4O_2$, Sigma-Aldrich), 1,2 dichloroethane 99.8% ($ClCH_2CH_2Cl$, Sigma-Aldrich), were used as received for electrochemical measurements. Data were acquired using a Solarton 1470 potentiostat and Corrview software.

The synthesised perovskite films of methyl ammonium lead iodide ($MAPbI_3$) and cesium lead bromide ($CsPbBr_3$) on FTO were used as working electrodes exposed to the electrolyte solution of tetrabutylammonium hexafluorophosphate (NBu_4PF_6) in dichloroethane $C_2H_4Cl_2$. All the electrochemical and photoelectrochemical measurements were carried out at room temperature in a sealed electrochemical cell.

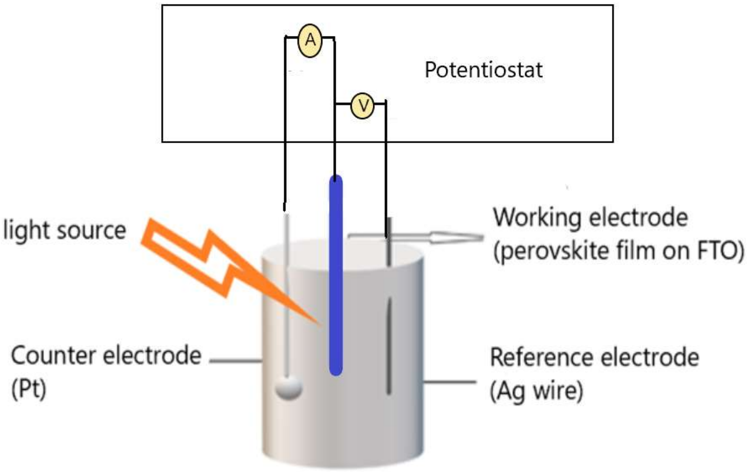

Figure 3.1 Photoelectrochemical cell for studing the photoactivity of perovskite.

As the perovskite materials are sensitive to humidity, the electrochemical and photoelectrochemical measurements were carried out in a customized sealed electrochemical cell that includes two ports to control gas flow through the cell. The cells were degassed using Ar for a minimum of 10 minutes prior to beginning measurements and a constant Ar cloud was maintained during measurements. The surface area of the electrode exposed to the electrolyte was defined in this cell as 0.07 cm^2.

Electrochemical impedance meausurements and photoelectrochemical measurements were carried out in the custom electrochemical cell using a Biologic (SP-300) potentiostat and the results were analysed by the EC-Lab application. A white light source LED was used for photoelectrochemical measurements, and the intensity was determined to be 15 mW/cm^2 using a power meter.

CHAPTER IV

RESULTS AND DISCUSSION

This chapter focuses on the preparation and characterization of thin films of a hybrid organic-inorganic $MAPbI_3$ perovskite and an all inorganic $CsPbBr_3$ perovksite. Thin film characterization was done using XRD, UV-visible absorption and SEM. After optimization of the thin film preparation linear sweep voltammetry measurements were carried out to determine the electrochemical stability window the $MAPbI_3$ and $CsPbBr_3$ thin films in 0.1 M $TBAPF_6$ in dichloroethane. Photoelectrochemical measurements were carried out in the absence and in the presence of a redox mediator ($BQ/BQ^{\cdot -}$) to determine the photocurrent efficiency of the photoelectrodes. Electrochemical impedance spectroscopy measurements were carried out to determine the bulk and interfacial parameters of the lead halide perovskite electrodes.

4.1 Methylammonium lead iodide ($MAPbI_3$)

The electrodeposition of $MAPbI_3$ has been carried out by several groups on a variety of substrates. It is a multi-step process that involves the electrodeposition of PbO_2 followed by one or two chemical conversion steps. (Chen *et al.*, 2015; Koza *et al.*, 2016;

Popov *et al.*, 2016). The anodic electrodeposition of PbO_2 is given by the following reaction:

$$Pb^{2+}(aq) + 2H_2O(l) \longrightarrow PbO_2(s) + 4H^+ + 2e^- \qquad (1)$$

Once the PbO_2 film is obtained on a conductive substrate it can be chemically converted in one step to $MAPbI_3$ or it can be converted in two steps by converting it to PbI_2 and then $MAPbI_3$. These steps can be carried out in the liquid or vapor phase. In this work, $MAPbI_3$ thin films were prepared using a one step chemical conversion of PbO_2 in solution.

Effect of electrodeposition time on PbO_2 film thickness:

By optimizing the conditions of electrodeposition, it is possible to control the uniformity of the film. The optimum result for the electrodeposition of PbO_2 was achieved at 0.25 mA cm^{-2} current density (Georgi Popov, 2015) on FTO substrates. They found that this to be the highest current density possible without creating non-uniform regions. In this work, PbO_2 was electrodeposited on FTO for different times between 100s and 900s. Electrodeposition for longer time shows less transparency as seen by the change in the intensity of the brown colour of the PbO2 on FTO substrate (Figure 4.1). As the electrodeposition time increases, the film becomes darker indicating an increase in the amount of PbO_2 on the substrate surface.

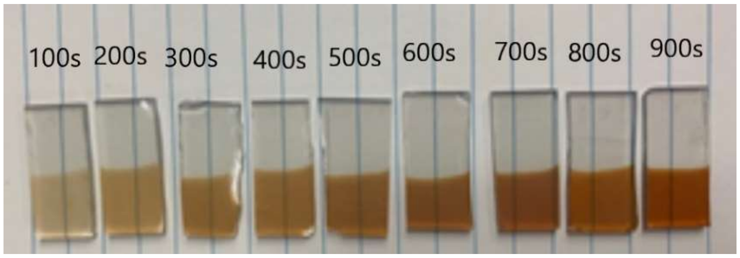

Figure 4.1 PbO_2 films on FTO for different electrodeposition times.

The thickness of the PbO_2 films was measured by two methods: the amount of charge passed during the electrodeposition and using a profilometer (Table 4.1). The thickness of the lead dioxide film depends on the time of deposition up to 600 seconds of electrodeposition time. After this time, the thickness of the film, as measured using a profilometer, plateaus at a thickness of about 170 nm (Figure 4.2).

Table 4.1 Thickness of the lead dioxide film on FTO (nm) measured by profilometer and the charge that passed during the electrodeposition

	Electrodeposition time (second)								
	100	200	300	400	500	600	700	800	900
Tickness of PbO_2 (nm) measured by profilometer	54	66	89	111	142	167	171	176	195
Tickness of PbO_2 (nm) measured by the amount of charge	27	55	112	115	150	220	243	247	312

The thickness of the film, using the amount charge passed with time, is predicted to increase using a galvanostatic electrodeposition method whereas profilometry measurements show that film thickness plateaus after 600 s. The thickness of the film, using the amount charge was calculated according to equation 1.3. The current density was constant for each electrodeposition while the surface area of the electrode was slightly different in each measurement. The continuous colour change of the films with electrodeposition time suggests that more PbO_2 is being deposited on the film beyond 600 s. This is also confirmed by an increase in absorption in the UV-Vis spectra presented in Figure 4.3. Although the film thickness does not increase beyond 600s, the amount of PbO_2 on the substrate does increase, suggesting the formation of a more dense film.

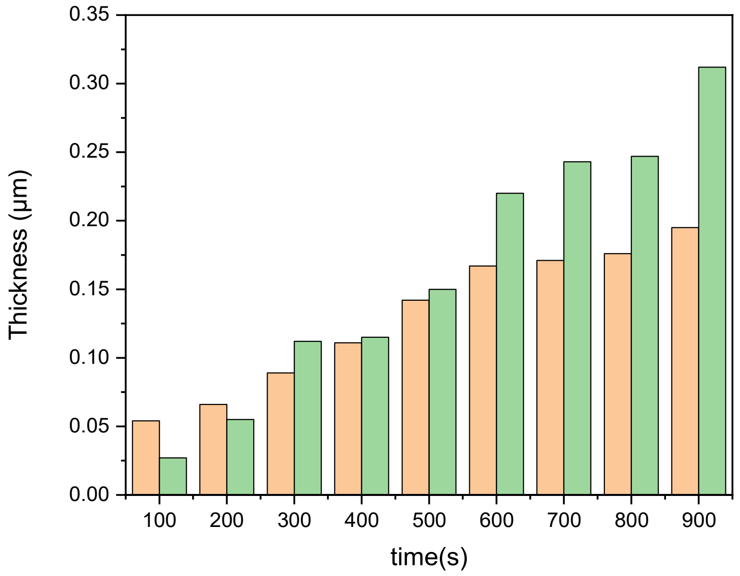

Figure 4.2 Comparison of the thickness of the PbO_2 film on FTO measured by profilometry (orange columns) and the amount of charge passed (green columns).

The morphology and uniformity of the film were observed by SEM and images of the PbO_2 film deposited at 300s, 500s , and 900s are presented in Figure 4.4. The film deposited at 900s is more uniform and shows full coverage consistent with the formation of a more dense and compact film.

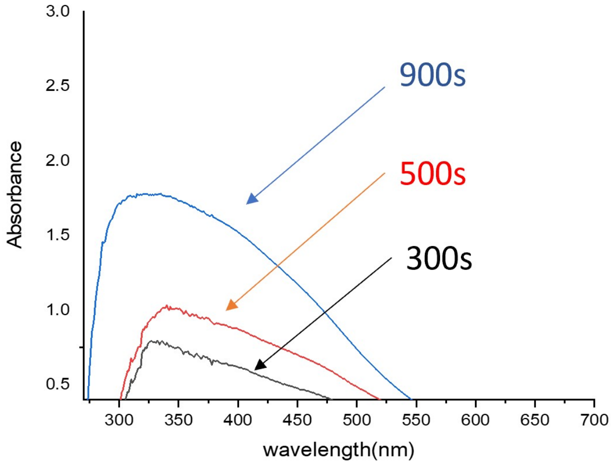

Figure 4.3 UV-Visible absorption of PbO_2 film electrodeposited at 900s (blue curve), 500s (red curve), 300s (black curve).

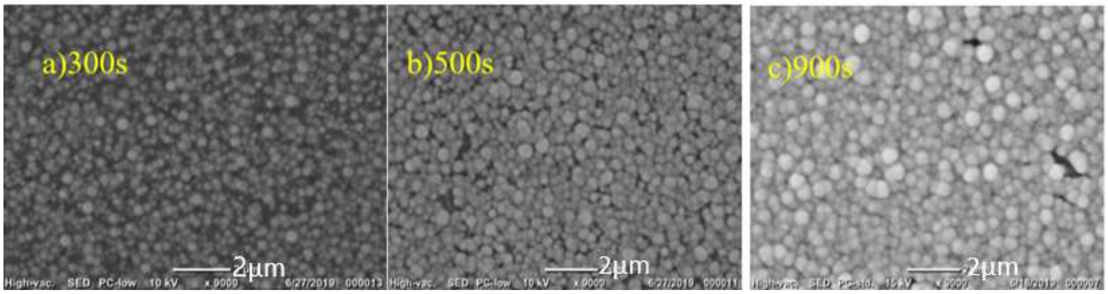

Figure 4.4 SEM images of PbO_2 electrodeposited at a) 300s, b) 500s, c) 900s.

Once a series of PbO_2 substrates were prepared, a variety of conditions for the chemical conversion of PbO_2 to $MAPbI_3$ were explored to optimize the final perovskite film quality and surface coverage. Until now, there has not been a systematic study of the one step chemical conversion of PbO_2 to $MAPbI_3$ as a function of the amount of PbO_2, the concentration of MAI used for chemical conversion or the length of conversion time. These variables are explored further in the following sections.

4.1.1 Effect of the time of coversion on the $MAPbI_3$ film quality

To verify that the optimum film of PbO_2 is chosen for the conversion to $MAPbI_3$, three films of PbO_2 that were electrodeposited at 300s, 500s, and 900s were used for chemical conversion. These films were immersed in a 0.05 M methylammonium iodide (MAI) solution in iso-propanol for chemical conversion times of 5 minutes, 15 minutes, and 30 minutes. The colour of the films changes from brown to black during the chemical conversion. The SEM images in Figure 4.5 show the formation of more compact films after 30 minutes of conversion. After 5 minutes we still observe PbO_2 particles on the substrate along with a low density of $MAPbI_3$ crystals.

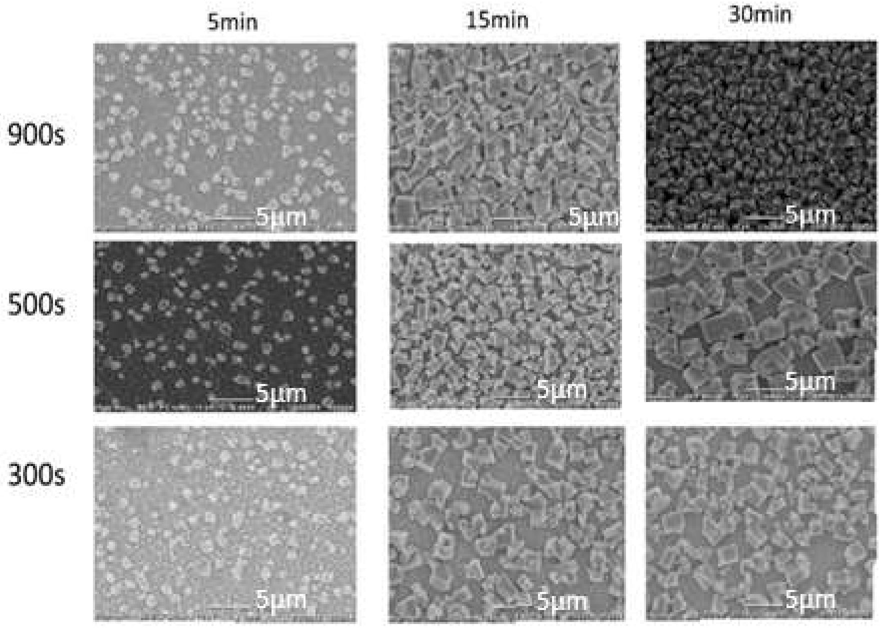

Figure 4.5 SEM images of $MAPbI_3$ converted in 5 minutes, 15 minutes , and 30 minutes for the three different PbO_2 films that electrodeposited in 300s, 500s, and 900s.

The $MAPbI_3$ film converted for 30 minutes shows the most uniform coverage of $MAPbI_3$ when using PbO_2 that was electrodeposited for 900s. This indicates that a critical amount of Pb must be available on the subsrate in order to obtain complete surface coverage of $MAPbI_3$. Subsequently, the $MAPbI_3$ films converted for 30 minutes were characterized by XRD to evaluate the structure of the final films (Figure 4.6).

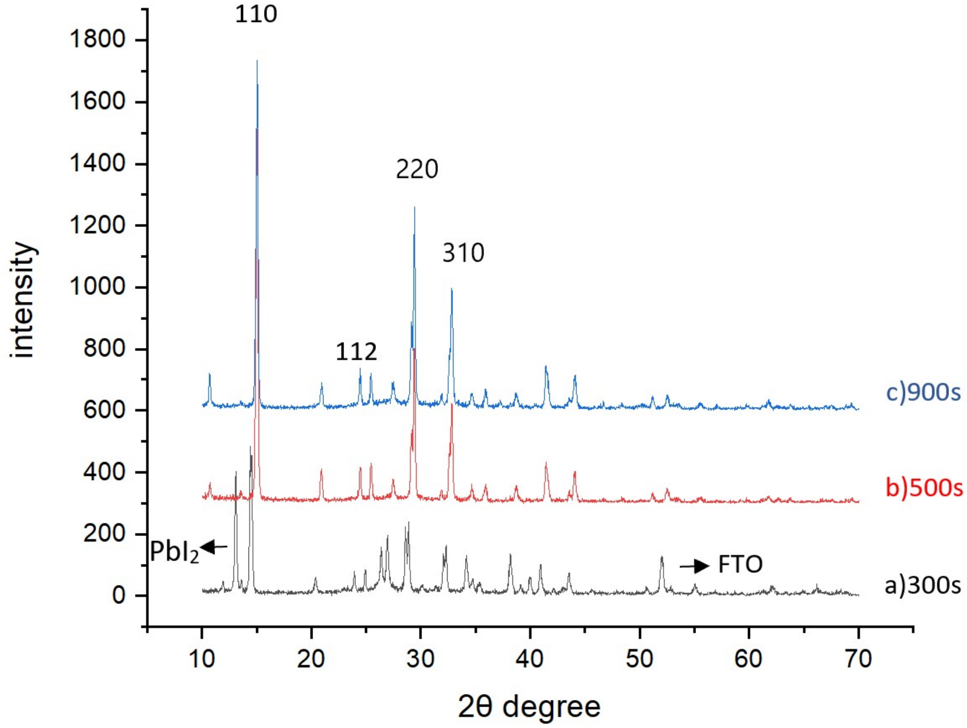

Figure 4.6 Diffractograms of $MAPbI_3$ prepared using PbO_2 films electrodeposited at 300 seconds (black diffraction pattern), 500s (red diffraction pattern), and 900s (blue diffraction pattern). All three films were chemically converted for 30 minutes in 0.05 M, MAI solution.

The XRD peaks recorded at (110), (112), and (220) confirm the chemical conversion to $MAPbI_3$ and correspond to the tetragonal $MAPbI_3$ perovskite crystal structure (Georgi Popov, 2015). The peak intensity increases for films converted using longer electrodeposition times consisntent with higher perovskite coverage on the FTO substrate.

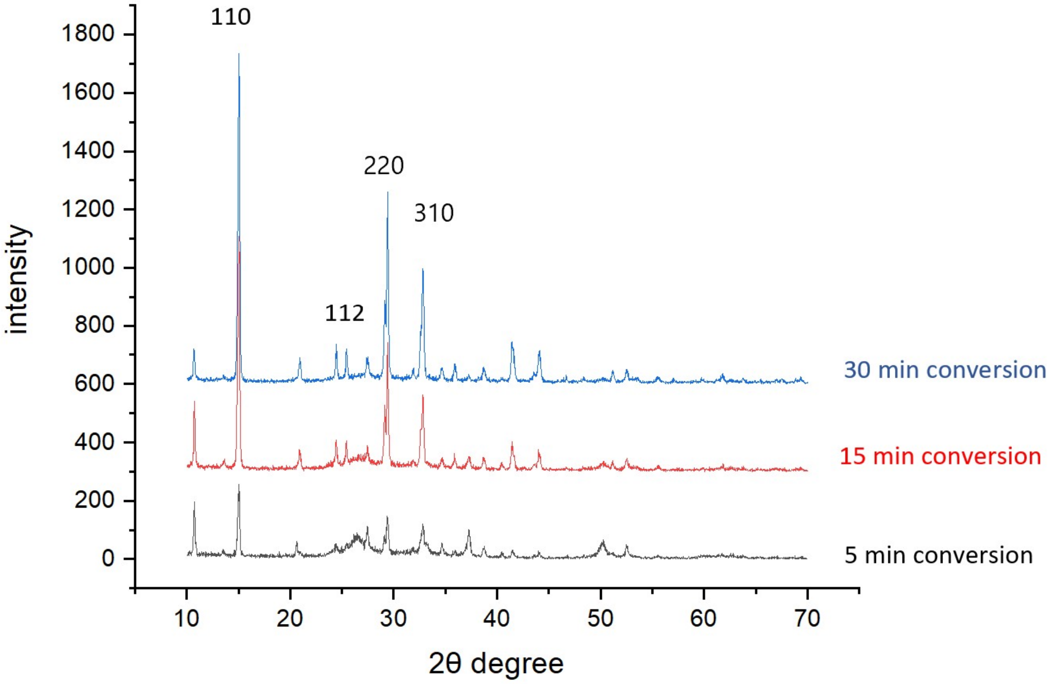

Figure 4.7 Diffractograms of $MAPbI_3$ coverted for 5 minutes (black diffraction pattern), 15 minutes (red diffraction pattern), and 30 minutes (blue diffraction pattern) for PbO_2 electrodeposited for 900 seconds in (0.05M) MAI solution.

SEM images of $MAPbI_3$ for the chemical conversion at three different times of 5, 15, and 30 minutes (Figure 4.5) show a higher surface coverage of the perovskite film for longer conversion times, which is consistent with the XRD measurements (Figure 4.7) that show more intense diffraction peaks for longer conversion times. The diffraction peaks that appear at (110), (112), and (220) are due to the tetragonal $MAPbI_3$ crystal structure and are not well defined after 5 minutes of chemical conversion. After 15 minutes of chemical conversion, the diffraction peaks become more pronounced and after 30 minutes the peaks are sharp and intense which is evidence for the formation of $MAPbI_3$ perovskite.

4.1.2 Chemical conversion in different concentration of methylammonium iodide (MAI)

The perovskite film of $MAPbI_3$ in this research work was prepared by the one-step chemical conversion by immersing the PbO_2 film on FTO in MAI solution. The effect of the concentration of the MAI solution in iso-propanol was studied by immersing the PbO_2 film in three different concentrations of MAI solution in iso-propanol (0.2 M, 0.1 M, and 0.05 M) for either 30 minutes or 60 minutes.

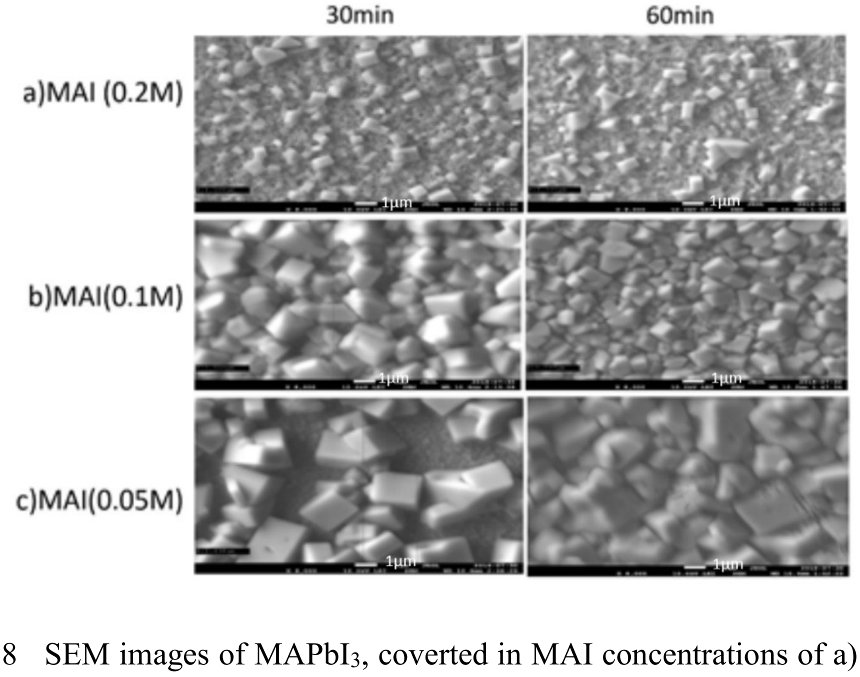

Figure 4.8 SEM images of $MAPbI_3$, coverted in MAI concentrations of a) 0.2 M, b) 0.1 M, and c) 0.05 M for 30 minutes and 60 minutes.

The SEM images of the final $MAPbI_3$ films are presented in Figure 4.8. The morphology of the film that was converted in 0.2 M MAI shows incomplete surface coverage that decreases when increasing the chemical conversion time from 30 minutes to 60 minutes. This suggests that too high a MAI concentration can lead to dissolution of the PbO_2 or $MAPbI_3$ resulting in poor surface coverage. By reducing the concentration of MAI solution to 0.1 M, more of $MAPbI_3$ is retained on the FTO substrate and covers a more complete area of the surface. Under these conditions, the film becomes more uniform and shows a compact morphology, however, the XRD of this film did not indicate complete conversion to $MAPbI_3$ (Figure 4.9). Again the MAI solution was diluted by a factor of two to a concentration of 0.05 M. SEM shows a compact and uniform film of $MAPbI_3$ for films converted at 0.05 M with the resulting film showing a larger particle size. For lower concentrations of MAI below 0.04M, the morphology of $MAPbI_3$ again showed incomplete conversion. Following these results, a concentration of 0.05 M MAI was considered optimal for converting the PbO_2 substrate.

The diffractograms of the three $MAPbI_3$ films (Figure 4.9) show higher crystallinity for the film that was converted with 0.05M MAI. The characteristic peaks of tetragonal $MAPbI_3$ at 14.38° (110), 28.5° (220), and 32.3° (310) are more intense for the film converted using 0.05M MAI which confirms the completed chemical conversion to $MAPbI_{3.}$

When perovskites are used in a solar cell or as a photocatalyst, it is important to have a uniform film with an optimal particle size and perovskite film thickness as these factors control the charge carrier length and light absorption which can directly affect the performance and efficiency of the films.

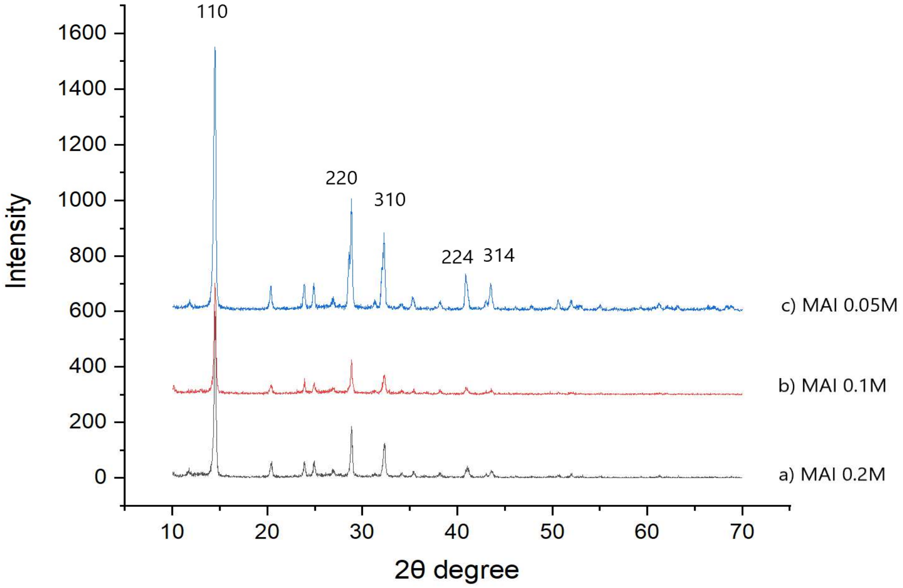

Figure 4.9 Diffractograms of $MAPbI_3$ converted using MAI concentrations of a) 0.2 M (black diffraction pattern), b) 0.1 M (red diffraction pattern) and c) 0.05M (blue diffraction pattern).

4.1.3 Effect of annealing on $MAPbI_3$ film

The as-prepared $MAPbI_3$ film was annealed at 100°C for 10 minutes to futher increase crystallization. The final film was characterized by XRD (Figure 4.10) and SEM (Figure 4.11). The intensity of the perovskite diffraction peaks of $MAPbI_3$ at (110), (220) and (310) increases following annealing. Both XRD plots exhibit the characteristic tetragonal $MAPbI_3$ diffraction pattern confiriming the chemical conversion is complete for both films, yet a higher crystallinity was obtained following annealing.

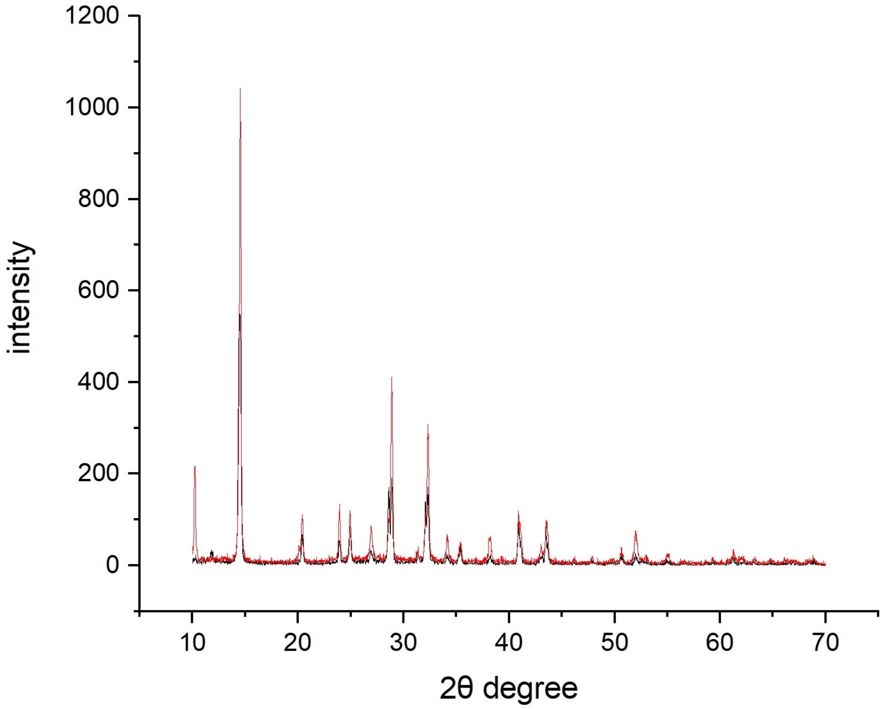

Figure 4.10 Diffractrograms of $MAPbI_3$ films prepared using PbO_2 electrodeposited for 900s and chemical conversion for 30 minutes in 0.05 M MAI before annealing (black diffraction pattern), and after annealing (red diffraction pattern).

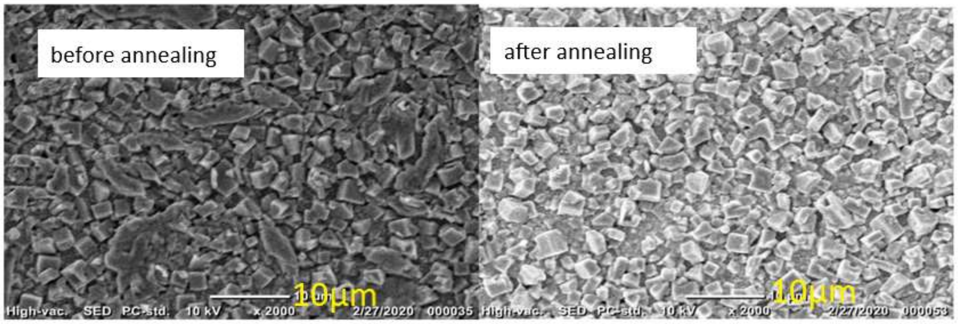

Figure 4.11 SEM of the $MAPbI_3$ film prepared using PbO_2 electrodeposited for 900s and chemical conversion for 30 minutes in 0.05 M MAI a) before annealing, and b) after annealing.

4.2 Cesium lead bromide ($CsPbBr_3$)

While there has been several exmples of the electrodepostion of $MAPbI_3$ perovskites, there has been very little work in the area of the electrodeposition of all-inorganic lead halide perovskites. Furthermore, to the best of our knowledge, there are no examples of the use of a two step chemical conversion of PbO_2 to $PbBr_2$ followed by complete conversion to $CsPbBr_3$. Instead, $CsPbBr_3$ has been obtained by passing through a PbI_2 intermediate instead of a $PbBr_2$ intermediate (Lv *et al.*, 2020). However, this could be a potential disadvantage if one wanted to control the $CsPbBr_3$ composition as residual iodide from PbI_2 could remain in the final perovskite thin film. As detailed in the experimental section (chapter 3) $CsPbBr_3$ on FTO was prepared by the electrodeposition of lead dioxide and followed by a two step chemical conversion, first from PbO_2 to $PbBr_2$ then by a second chemical conversion step to $CsPbBr_3$. Following the results of $MAPbI_3$ already presented, a PbO_2 time of 900s was chosen for chemical conversion. The effect of different times of conversion from $PbBr_2$ to $CsPbBr_3$ was studied to obtain a high surface coverage of the CsPbBr3 perovskite thin film.

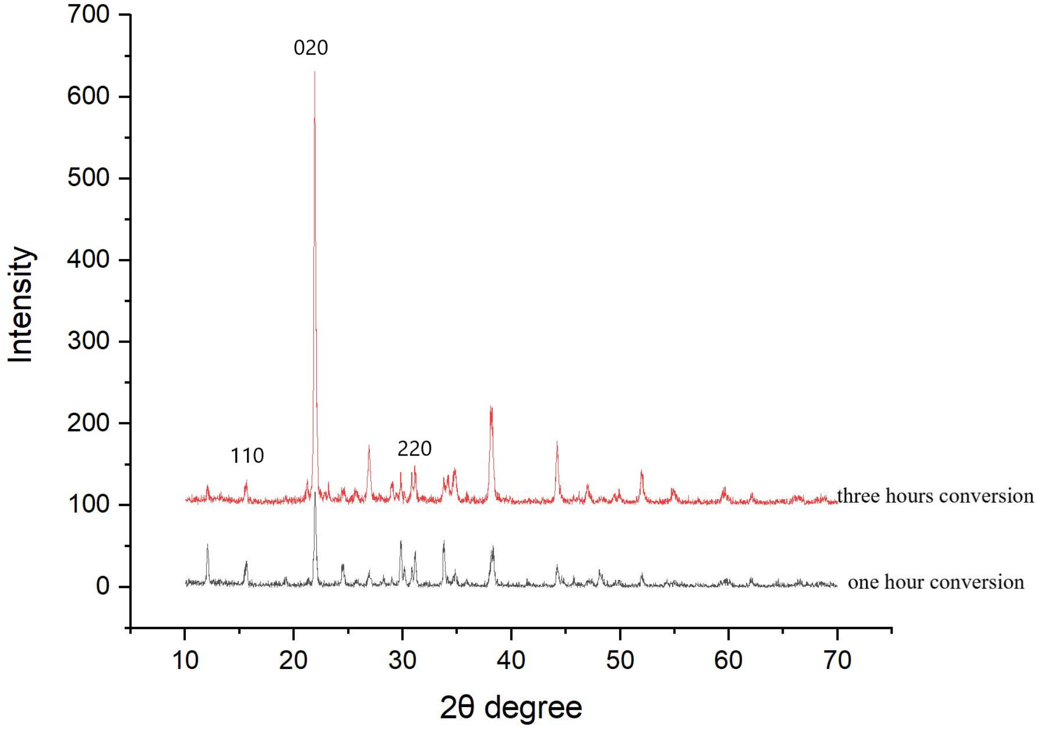

Figure 4.12 Diffractrograms of $CsPbBr_3$ chemically converted for one hour (black diffraction pattern) and for three hours (red diffraction pattern) in CsBr (0.02 M).

The orthorhombic phase has a diffraction pattern that shows characteristic peaks at 15.198°(110) and 30.663°(220) (Figure 4.12), which is evidence of orthorhombic for $CsPbBr_3$ crystals on the FTO substrate. The (110), (020) and (220) peaks for $CsPbBr_3$ converted for three hours confirm a completed chemical conversion with high crystallinity.

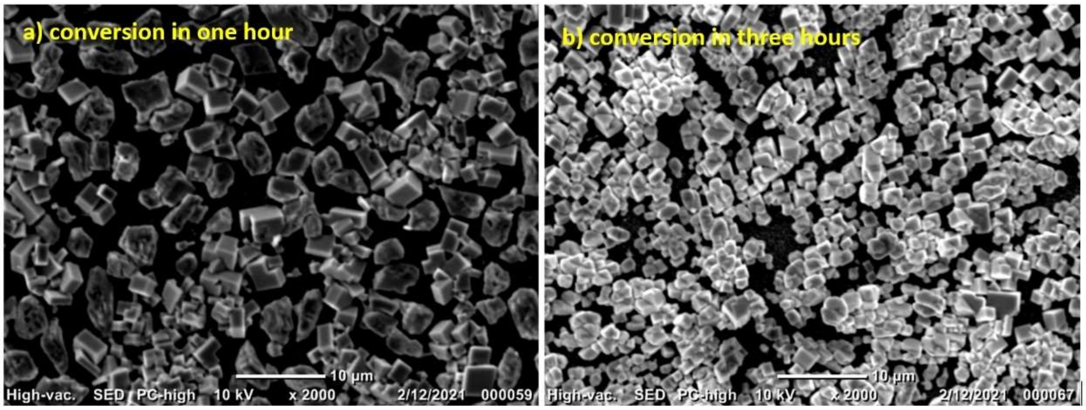

Figure 4.13 SEM images of $CsPbBr_3$ a) after one hour conversion (left), b) after three hours conversion (right).

The SEM images of both $CsPbBr_3$ films in figure 4.13 confirm the formation of crystalline particles with the film becoming more uniform and compact after three hours of chemical conversion.

4.3 Electrochemistry and photoelectrochemistry of $MAPbI_3$ and $CsPbBr_3$

Electrochemistry is a useful method that can be used to study the electrode behavior (perovskite film on FTO) in an electrolyte solution. Also, the behavior of electrodes in a photoelectrochemical cell can be used in the design of new photocatalytic systems as it provides a system to measure photoinduced charge transfer at the electrode/electrolyte interface by measuring the current that flows through the electrode under illumination. It can also provide information about the energy required to carry out a reaction by the potential needed to produce that amount of current with and without illumination in the study of the photoelectrochemical activity of our material.

4.3.1 Stability window of $MAPbI_3$ and $CsPbBr_3$

Lead halide perovskites are ionic materials and highly unstable in almost all solvents (Hsu *et al.*, 2015). To date most measurements have been carried out in dichloromethane. In this work dichloroethane was used due to its higher boiling point which enabled the electrochemical cell to be continuously purged for extended periods of time without considerable solvent evaporation. To find the stability window for the $MAPbI_3$ and $CsPbBr_3$, linear sweep voltammograms were carried out in NBu_4PF_6 / dichloroethane (DCE) and are presented in Figure 4.14 for $MAPbI_3$ and Figure 4.15 for $CsPbBr_3$.

Both the $MAPbI_3$ and CsPbBr3 films show the onset of a reduction peak at - 0.5 V vs Ag/Ag^+, and the onset of oxidation at + 0.4 V vs Ag/Ag^+. The onset of the anodic and cathodic currents have been attributed to the corrosion of the perovskite film (SamuScheidtKamat*, et al.*, 2018). For the anodic current the following corrosoion reaction has been proposed:

$$CsPbBr_3\,(s) \rightarrow PbBr_2\,(s) + Cs^+\,(aq) + 0.5\ Br_2\,(l) + e^- \qquad (2)$$

Followed by:

$$PbBr_2\,(s) \rightarrow Pb^{2+}\,(aq) + Br_2\,(l) + 2e^- \qquad (3)$$

While for the cathodic corrosion the following reaction has been proposed:

$$CsPbBr_3\,(s) + 2e^- \rightarrow Pb\,(s) + Cs^+ + 3Br^-\,(aq) \qquad (4)$$

As the corrosion processes are irreversible it was necessary to use a new film for the anodic and cathodic sweeps. The linear sweep voltammograms began from open circuit potential and were scanned out to either the maximum anodic or cathodic potential.

While the proposed mechanism was for $CsPbBr_3$ perovskites, it is assumed that a similar process occurs for the $MAPbI_3$ perovskite with the anodic oxidation leading to the formation of PbI_2 (s) and the cathodic corrosion leading to the formation of Pb(s), both of which are known degradation products in solid state perovskite solar cells.

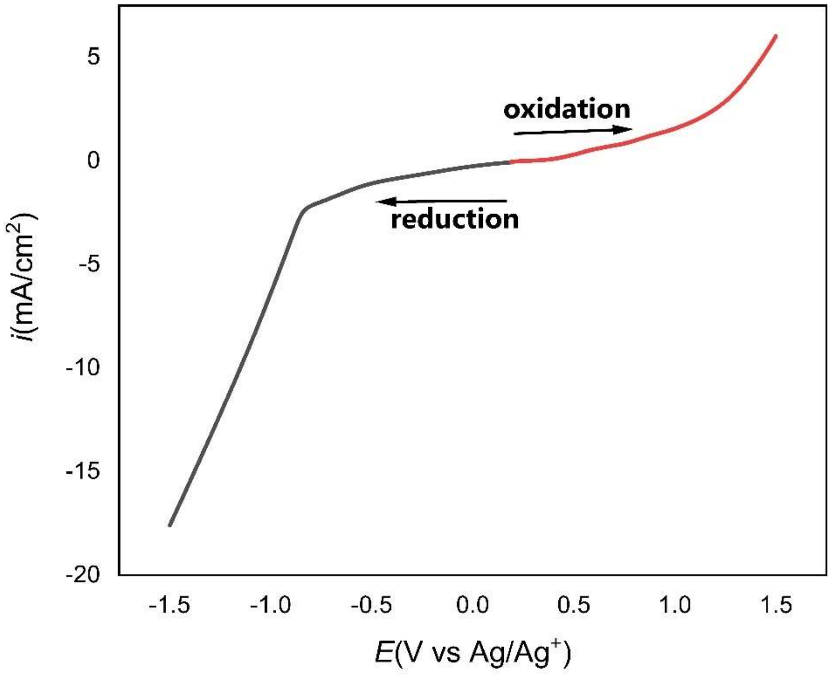

Figure 4.14 Linear sweep voltamogramme of FTO/$MAPbI_3$ in 0.05M NBu_4PF_6 in dichloroethane (DCE) with 10mv/s scan rate.

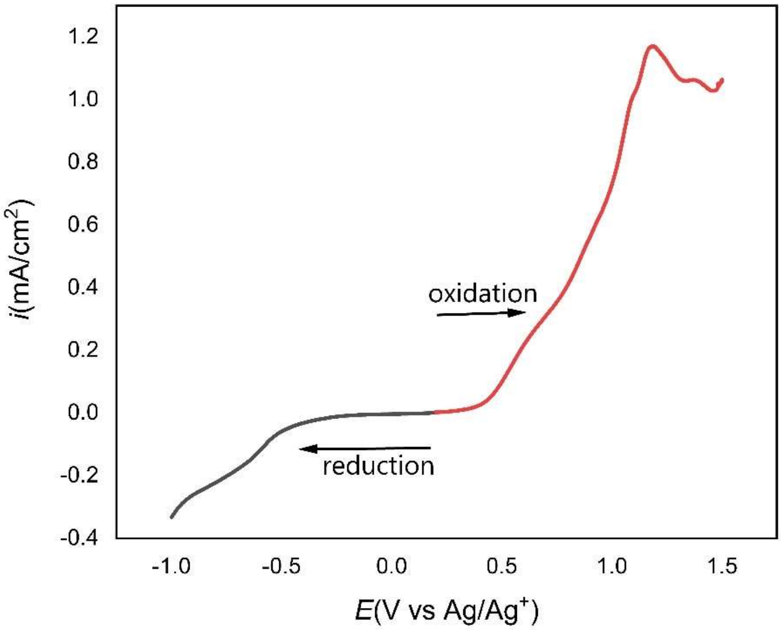

Figure 4.15 Linear voltamogramme of FTO/$CsPbBr_3$ in 0.05M NBu_4PF_6 in dichloroethane (DCE) with 10mv/s scan rate.

4.3.2 Photoelectrochemistrty of $MAPbI_3$ and $CsPbBr_3$

The photoelectrochemistry of lead halide perovskites is relatively unknown, in part due to the limited stability of these materials in most solvents and more importantly due to their rapid development as solid state photovoltaic materials. The leading materials for solar cells are based on the hybrid organic $MAPbI_3$ while research in the area of lead halide perovskites as photocatalysts has focused on $CsPbBr_3$. The all inorganic $CsPbBr_3$ has a larger bandgap, which can be useful for driving electrocatalytic reactions such as water oxidation, carbon dioxide reduction and hydrogen evolution. (Poli *et al.*, 2019) In the following section the photoelectrochemistry of electrodeposited $MAPbI_3$ and $CsPbBr_3$ are compared. Measurements were made using the redox mediator benzoquinone which has been shown to be an electron acceptor for perovskite based photocathodes (Hsu *et al.*, 2015). Measurements are also made in the absence of a redox mediator to detect any photodegradation of these materials that might contribute to the photocurrent response. In order to minimize the contribution of background corrosion to the measurements the potential window was limited between + 0.4 V and -0.2 V vs. a Ag wire quasireference electrode, which was shown to exhibit a plateau with minimal background current for both materials.

In figure 4.16 and 4.17 linear sweep voltammograms are presented for $MAPbI_3$ under illumination. Blank measurements, using only a supporting electrolyte of 0.05M NBu_4PF_6 are presented in Figure 4.16. The left hand figure presents the results for measurements in the dark (black trace) and under illumination (red trace). The right hand figure presents the net photocurrent, which is the difference in current measured under light and in the dark. Under illumination, a small anodic

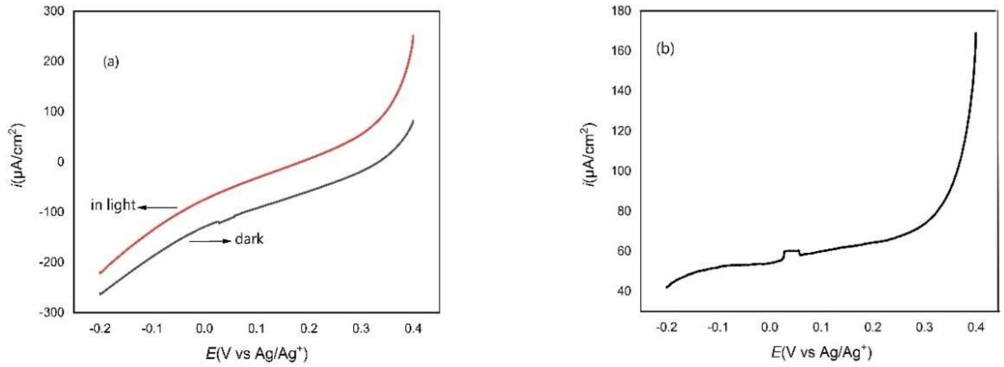

Figure 4.16 (a) Linear voltammogram of FTO/$MAPbI_3$ in 0.05M NBu_4PF_6 in dichloroethane (DCE) with 10mv/s scan rate, in dark (black), under illumination (red) . (b) net photocurrent density curve versus potential.

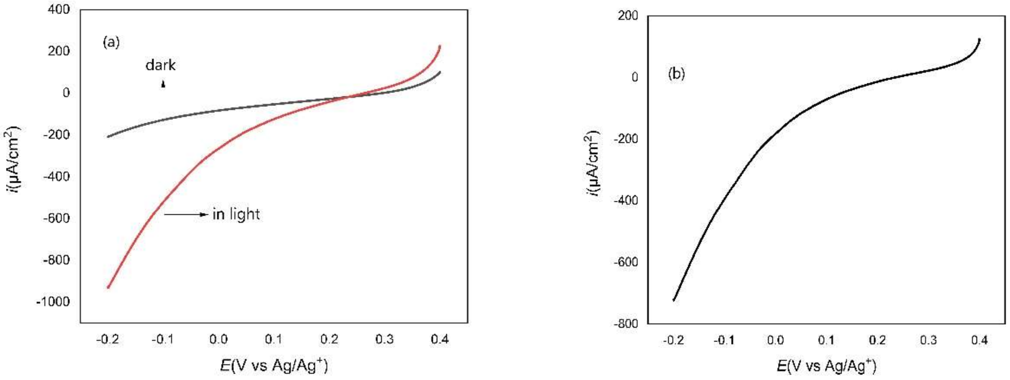

Figure 4.17 (a) Linear voltammogram of FTO/MAPbI$_3$ in 0.05M NBu$_4$PF$_6$ in dichloroethane (DCE) with 2mM benzoquinone in dark (black), under illumination (red) . (b) net current density curve versus potential

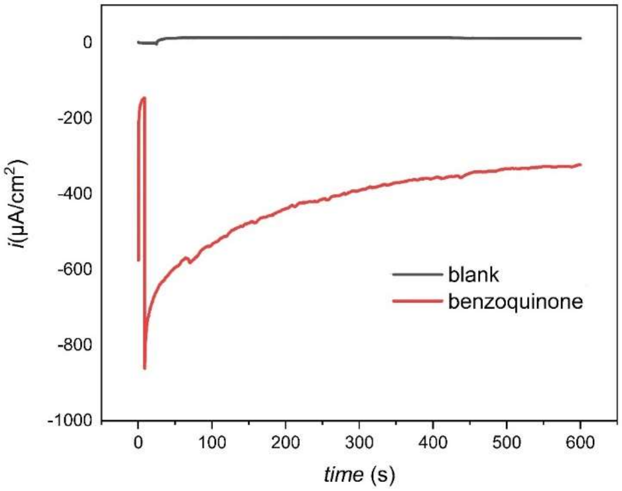

Figure 4.18 Time dependant photocurrent of FTO/MAPbI$_3$ in 0.05M NBu$_4$PF$_6$ in dichloroethane (DCE) at the constant potential -0.1V vs Ag/Ag+ black curve is blank, red curve with 2mM benzoquinone.

Photocurrent is observed for all potentials. The photocurrent could be due to photocorrosion following a similar mechanism to reaction 2 above and leading to the formation of PbI_2 (s). This possibility was supported by photocurrent measurements made for longer periods of time (Figure 4.18) where films were sometimes observed to have some yellow colour following extended photocurrent measurements. The yellow colour is characteristic of PbI_2 (s).

Figure 4.17 presents photocurrent measurements made using $MAPbI_3$ and benzoquinone as an electron acceptor to capture photogenerated electrons generateed by the p-type perovskite semiconductor materials. The photocurrent in this case was cathodic consistent with the photoreduction of the benzoquinone redox mediator and are in contrast with the blank measurements where an anodic photocurrnet was observed. Photocurrent measurements over an extended period of time (10 minutes) were made with and without the benzoquinone redox mediator(Figure 4.18). The blank measurement (black trace) shows an anodic photocurrent whereas measurements made in the presence of benzoquinone show a pronounced cathodic photocurrent that is much larger in magnitude. The photocurrent obtained with benzoquinone slowly decays over time falling to less than half its initial value under illumination. The large spike and subsequent decay of the photocurrent is characteristic of interfacial recombination.

Linear sweep voltammograms under illumination are presented in Figure 4.19 and Figure 4.20 for CsPbBr3 for the same conditions. The blank measurements (Figure 4.19) show a cathodic photocurrent, which is in contrast to the blank measurements for $MAPbI_3$. This suggests that anodic photocorrosion is less problematic in this potential range than for $MAPbI_3$. One possibility is that the cathodic photocorrosion occurs in this potential range. Another possibility is the presence of oxygen in the cell that could be reduced under illtumination. However, the cell is purged with oxygen prior to and during the measurements. For this reason, it is considered that cathodic photocorrosion is more pronounced for the $CsPbBr_3$. In the presence of benzoquinone the cathodic photocurrent is further enhanced. When comparing the total photocurrent under illumination for the blank measurement (Figure 4.19a) and the measurement with benzoquinone (Figure 4.20a) it can be seen that the photocurrent is approximately 50% larger in the presence of benzoquinone. However, when comparing the net photocurrent density between the blank measurement (Figure 4.19b) and benzoquinone measurement (Figure 4.20b) it can be seen that at the most negative potential (ca. -0.2 V) the photocurrent values are much closer in value whereas for more positive potentials a more significant difference in the photocurrent values can be observed. In fact the net cathodic photocurrent is relatively constant across all potential values in the presence of benzoquinone. The similar value of the net photocurrent at more negative potentials is attributed to an important background current due to the benzoquinone reduction by the underlying FTO electrode. The dark current for the benzoquinone sample is much larger than the blank sample indicating that benzoquinone can be reduced in the dark on the underling FTO substrate. It is not

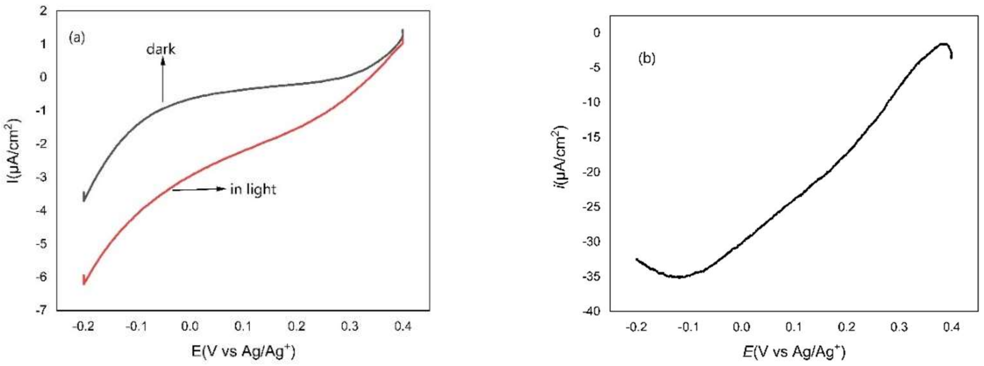

Figure 4.19 (a) Linear voltammogram of FTO/$CsPbBr_3$ in 0.05M NBu_4PF_6 in dichloroethane (DCE) (black), under illumination (red). (b) net current density curve versus potential

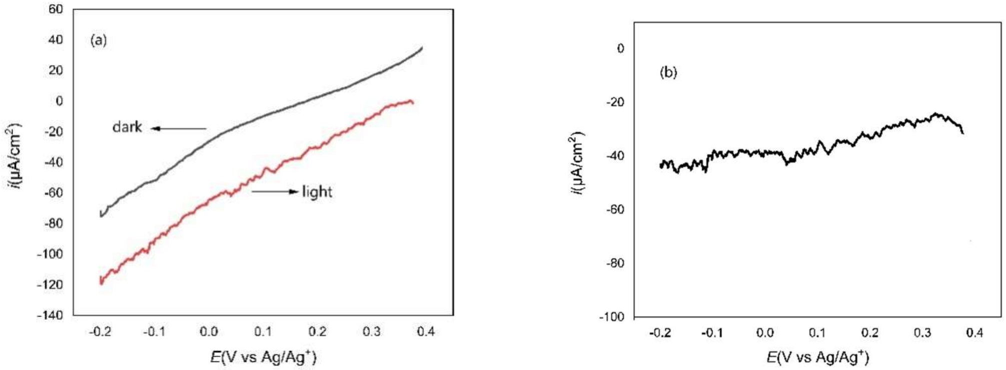

Figure 4.20 (a) Linear voltammogram of FTO/$CsPbBr_3$ in 0.05M NBu_4PF_6 in dichloroethane (DCE) with 2mM benzoquinone (BQ) in dark (black), under illumination (red). (b) net current density curve versus potential

expected that $CsPbBr_3$ will reduce benzoquinone as it is a p-type semiconductor. Also comparing the dark currents measured for $MAPbI_3$ under blank conditions and with benzoquinone show that no difference was observed between the two samples. This suggests that a portion of the FTO sample remains exposed to the electrolyte for $CsPbBr_3$ whereas the $MAPbI_3$ has a more complete coverage across the FTO surface. This is consistent with the differences observed in SEM where the underlying FTO substrate could be observed for the $CsPbBr_3$ samples. A white light source was used for illumination and $CsPbBr_3$ (2.2 eV) has a larger bandgap than $MAPbI_3$ (ca. 1.5 eV) which explains why the photocurrent is smaller for the $CsPbBr_3$ material.

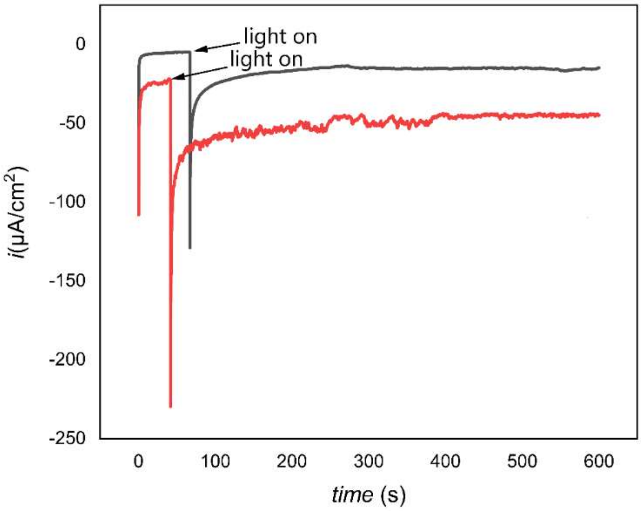

Figure 4.21 Time dependent photocurrent of FTO/ $CsPbBr_3$ in 0.05M NBu_4PF_6 in dichloroethane (DCE) at the constant potential -0.1V vs Ag/Ag+ blank (black) and with 2mM benzoquinone (red).

Photocurrent transient measurements obtained at a constant potential of -0.1 V are presented in Figure 4.21 for $CsPbBr_3$ using a benzoquinone redox mediator. The photocurrent shows a sharp spike following illumination similar to $MAPbI_3$. However, the $CsPbBr_3$ shows a more rapid decay in the photocurrent before reaching a plateau. In addition, the fraction of the photocurrent that remains in the plateau region is considerably less than for $MAPbI_3$ indicating that the interfacial recombination is even more pronounced for the $CsPbBr_3$ sample.

4.4 Electrochemical impedance spectroscopy

Electrochemical impedance spectroscopy was used to study $MAPbI_3$ and $CsPbBr_3$ in the dark and under illumination in the presence of a benzoquinone redox mediator. The measurements were carried out as a function of the electrode potential in the same potential window that was used for photoelectrochemical measurements. The data were fit using the equivalent circuit shown in Figure 4.22 and representative Nyquist and Bode plots for $MAPbI_3$ and $CsPbBr_3$ are presented in Figure 4.23.

The equivalent circuit used to fit the impedance data included 5 different elements composed of resistors (R1, R2, R3) and constant phase elements (Q1, Q3). Following the assignment of Guerrero *et al*, the physical meaning of each element are a series resistance (R1), a shunt resistance (or recombination resistance) in the perovskite bulk (R2), interfacial charge transfer (R3), geometric capacitance (Q1) and interfacial capacitance (Q3). (Guerrero *et al.*, 2021) The constant phase element does not correspond to a capacitance and needs to be transformed through the following relationship: $C = (RQ)^{1/\alpha}/R$.

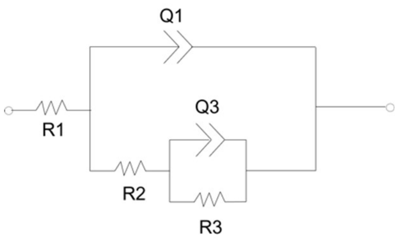

Figure 4.22 The equivalent circuit used to fit the EIS data

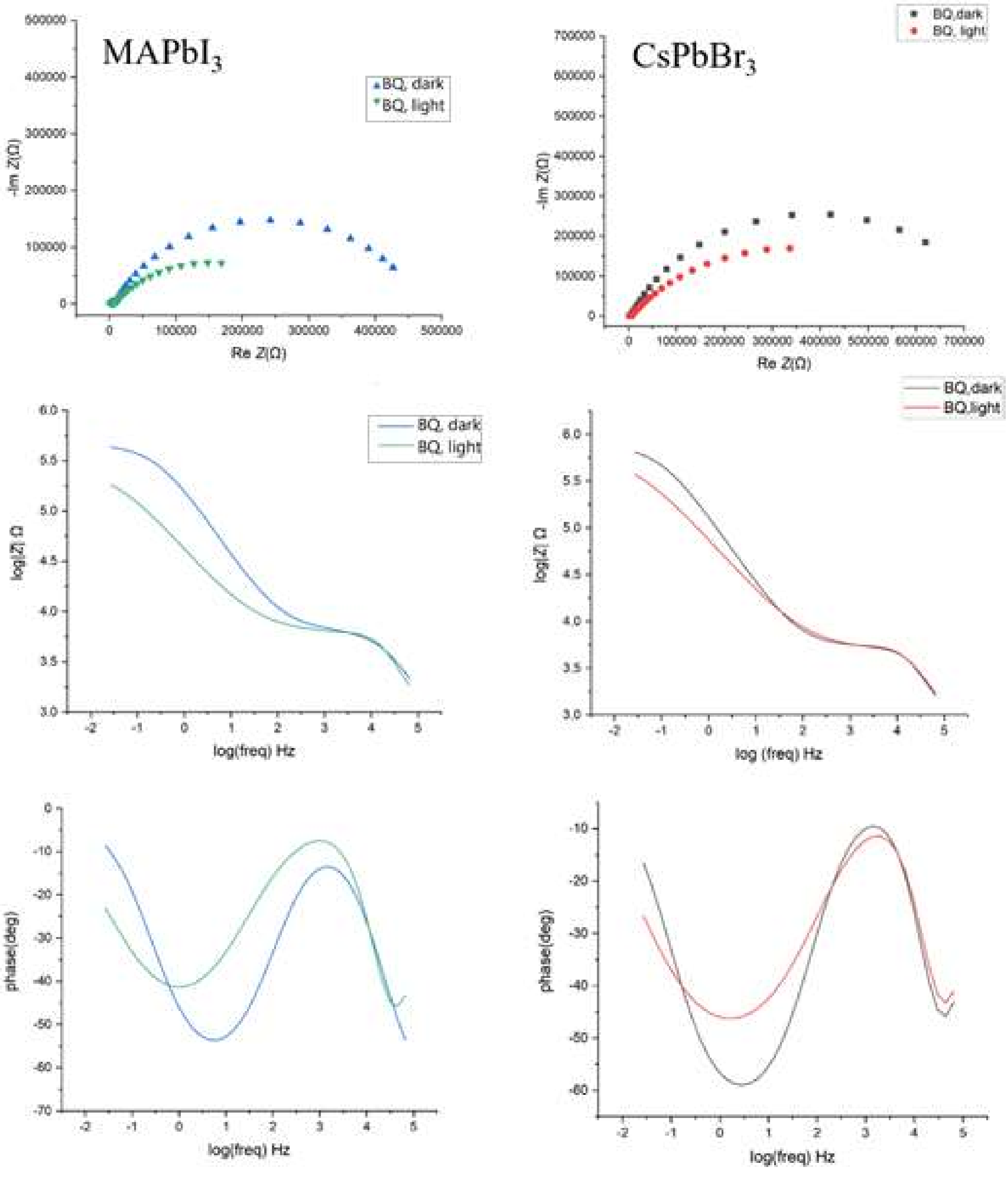

Figure 4.23 Nyquist and Bode plots at + 0.1 V for $CsPbBr_3$ and $MAPbI_3$ in 0.05M NBu_4PF_6 in dichloroethane (DCE) at the constant potential -0.1V vs Ag/Ag+ in the dark and under illumination.

The Nyquist plots show two semicircles, one small high frequency near the origin followed by a second and much larger semicircle at lower frequencies. The high frequency semicircle is due to the bulk of the perovskite film while the low frequency semicircle arises from the perovskite/electrolyte interface. The size of the $MAPbI_3$ and $CsPbBr_3$ semicircles at low frequency both decrease in size following illumination due to an increased photoinduced charge transfer at the perovskite/electrolyte interface. The parameters used to fit the impedance data are presented in Tables 4.2 – 4.5.

Focusing first on the high frequency semicircle, it can be seen that the series resistance of the cell, R1, remains constant for all samples and is primarily determined by the electrolyte conductivity, which is quite low being an organic solvent and low supporting electrolyte concentration of 50 mM to minimize the perovskite degradation. Any minor difference between measurements is attributed to the placing of the reference electrode in the photoelectrochemical cell. The shunt resistance (R2) was found to be consistently higher for $MAPbI_3$ than $CsPbBr_3$ which is consistent with this material exhibiting enhanced photocurrent activity. This parameter, R2, represents the recombination resistance under illumination and once again the trend is the same for the two materials. The Q1 parameter showed some variation between the two materials in the dark and under illumination. The value of $\alpha 1$ is almost equal to 1 in all cases demonstrating that it behaves almost as a true capacitance. When the capacitance was calculated it was found to be in the range of 35 nF cm^{-2} which is comparable to geometric capacitance values of 40 nF cm^{-2} obtained for perovskite materials using impedance spectroscopy of solid state devices. (Aranda *et al.*, 2019)

Table 4.2 EIS fitting parameters for $MAPbI_3$ in the dark

E / V	R1 / Ω	Q1	α1	R2 / Ω	Q3	α3	R3 / Ω
-0.2	1064	5.63E-08	0.93	6183	1.13E-05	0.82	137663
-0.1	1056	5.46E-08	0.94	6145	1.15E-05	0.82	1.60E+05
0	1061	5.33E-08	0.94	6093	1.15E-05	0.83	1.93E+05
0.1	1140	3.83E-08	0.97	5898	1.26E-05	0.82	2.37E+05
0.2	1063	5.14E-08	0.94	6029	1.33E-05	0.81	2.82E+05
0.3	1098	4.40E-08	0.96	5915	1.48E-05	0.8	3.08E+05
0.4	1121	4.01E-08	0.96	5840	1.56E-05	0.8	2.64E+05

Table 4.3 EIS fitting parameters for $MAPbI_3$ under illumination

E / V	R1 / Ω	Q1	α1	R2 / Ω	Q3	α3	R3 / Ω
-0.2	978	4.99E-08	0.94	6152	6.76E-05	0.73	14763
-0.1	933	4.24E-08	0.95	5892	6.40E-05	0.72	2.31E+04
0	984	4.07E-08	0.96	5756	8.31E-05	0.68	9.21E+04
0.1	958	4.17E-08	0.96	5659	8.23E-05	0.68	1.13E+05
0.2	946	4.14E-08	0.96	5554	8.91E-05	0.67	1.11E+05
0.3	906	4.56E-08	0.95	5496	9.16E-05	0.67	8.40E+04
0.4	920	3.99E-08	0.97	5345	9.17E-05	0.67	6.16E+04

Table 4.4 EIS fitting parameters for $CsPbBr_3$ in the dark

E / V	R1 / Ω	Q1	α1	R2 / Ω	Q3	α3	R3 / Ω
-0.2	888	4.23E-08	0.97	5018	2.20E-05	0.83	173078
-0.1	880	4.29E-08	0.97	5017	1.77E-05	0.85	2.63E+05
0	875	4.37E-08	0.97	5012	1.63E-05	0.86	3.01E+05
0.1	879	4.36E-08	0.97	4988	1.60E-05	0.86	3.33E+05
0.2	886	4.11E-08	0.97	4957	1.50E-05	0.86	3.65E+05
0.3	869	4.36E-08	0.97	4971	1.41E-05	0.87	3.81E+05
0.4	866	4.43E-08	0.97	4964	1.39E-05	0.87	4.06E+05

Table 4.5 EIS fitting parameters for $CsPbBr_3$ under illumination

E / V	R1 / Ω	Q1	α1	R2 / Ω	Q3	α3	R3 / Ω
-0.2	958	3.99E-08	0.97	5055	3.50E-05	0.757	55202
-0.1	1032	4.29E-08	0.97	4941	2.50E-05	0.79	6.98E+04
0	937	4.06E-08	0.97	5001	2.20E-05	0.81	8.04E+04
0.1	1037	3.87E-08	0.98	4849	1.99E-05	0.82	8.91E+04
0.2	921	4.14E-08	0.97	4937	1.90E-05	0.83	9.77E+04
0.3	908	4.21E-08	0.97	4937	1.83E-05	0.83	9.76E+04
0.4	887	4.47E-08	0.97	4928	1.89E-05	0.83	9.97E+04

The fitting parameters for the low frequency semicircle R3 and Q3 are plotted in Figure 4.24 and Figure 4.25, where R3 represents interfacial charge transfer. In the dark, it can be seen that this value decreases with decreasing potential. The charge transfer resistance was found to be somewhat higher in the $CsPbBr_3$ sample in the dark. The origin of this difference is attributed to the enhanced corrosion rate of the $MAPbI_3$ film even in blank conditions compared with the $CsPbBr_3$ sample. These differences persist under illumination with the $MAPbI_3$ showing a slightly lower value of the charge transfer resistance. The smaller difference in the value of the charge transfer resistance under illumination might suggest that $CsPbBr_3$ exhibits improved kinetics for charge transfer even if the overall magnitude of the photocurrent is lower. The lower photocurrent value was attributed to differences in the bandgap values and the use of a white light source. Finally, the parameter Q3 is plotted as a function of the electrode potential and shows quite a striking difference in the $MAPbI_3$ sample in the dark and under illumination. The value of Q3 is almost one order of magnitude larger under illumination. When calculating the value of the capacitance, it was found to be approximately 20 μF cm^{-2} in the dark, which is a reasonable value for the electrochemical double layer. On the otherhand, under illumination the interfacial capacitance jumps to as much as 276 μF cm^{-2}. This phenomenon has been observed inperovskite photovoltaic devices with an unknown interpretation. Some possibilities include the build up of majority carriers at the interface or alternatively to a chemical reaction between the electrode contact and iodide in the $MAPbI_3$. In the case of the photoelectrochemical measurements, the second hypothesis is consistent with photocorrosion occurring at the interface. However, the build of majority carriers cannot be ruled out as there is no charge selective contact between the FTO substrate and perovskite material.

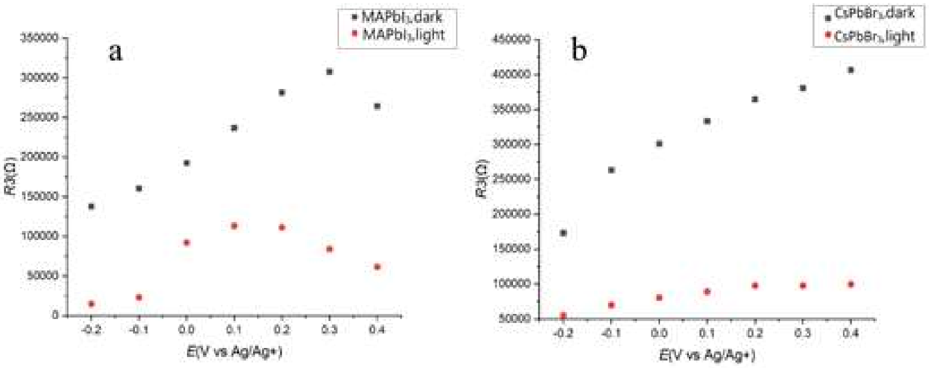

Figure 4.24 Resistance values as a function of applied potential for $CsPbBr_3$ and $MAPbI_3$ in dark and under illumination

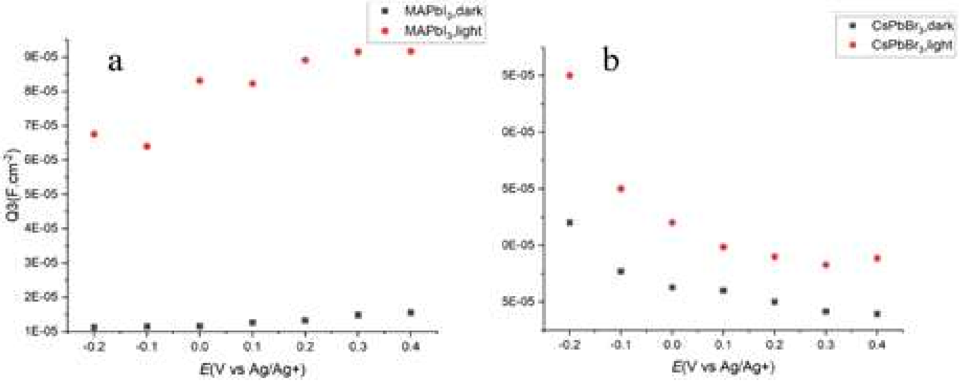

Figure 4.25 Capacitance values as function of applied potential for $CsPbBr_3$ and $MAPbI_3$ in dark and under illumination

When examining the values of Q3 for the $CsPbBr_3$, it was found that the calculated interfacial capacitance increased by a factor of two from 15 μF cm^{-2} in the dark to 30 μF cm^{-2} under illumination. This difference is less pronounced in $CsPbBr_3$ and is consistent with this material showing an overall lower rate of chemical reactivity at the interface.

CONCLUSION

In this work, electrodeposition of PbO_2 onto a FTO substrate followed by either a one step or two step chemical conversion in solution was used to obtain $MAPbI_3$ and $CsPbBr_3$ perovskite films. This work represents the first example of electrodeposition for the formation of $CsPbBr_3$ without the use of a PbI_2 intermediate. The synthesis method is an important step as the particle size and uniformity of the substrate coverage can affect the optoelectronic properties of the perovskite material. In conclusion, electrodeposition provided a reproducible method to form thin films of perovskites on a FTO electrode. Furthermore, we could control the thickness of the film by adjusting the duration of electrodeposition. Consequently, the morphology of the film could be controlled by altering the electrodeposition parameters. For that reason, the effect of time of deposition was studied and the morphology and the particle size of the final PbO_2 film were investigated using SEM. Moreover, the effect of salt concentration and time of conversion were studied on the chemical conversion to $MAPbI_3$ and $CsPbBr_3$ using XRD and SEM to find the optimal condition for film uniformity and crystallinity. Overall, it was found that $MAPbI_3$ gave higher surface coverage than $CsPbBr_3$ and this is attributed to the long conversion times that is required during the two step chemical conversion of PbO_2 to $CsPbBr_3$.

In this study, we evaluated the stability window of the two selected lead halide perovskites of $CsPbBr_3$ and $MAPbI_3$ in (0.05M Bu_4NPF_6 in dichloroethane). The stability window was used for carrying out electrochemical and photoelectrochemical measurements and it was found that $MAPbI_3$ was found to show a higher rate of corrosion than $CsPbBr_3$ in an electrolyte solution.

Subsequently, the electrode/electrolyte interface of $CsPbBr_3$ and $MAPbI_3$ in an electrolyte solution was investigated with and without benzoquinone along with the effect of illumination using photoelectrochemistry and electrochemical impedance spectroscopy. When comparing $CsPbBr_3$ and $MAPbI_3$ liquid junction cells, it was found that $MAPbI_3$ shows an enhance photo-response under white light illumination due to its smaller bandgap. Both materials exhibited interfacial recombination, which represents a promising target for the improvement of their photoelectrochemical activity.

$MAPbI_3$ and $CsPbBr_3$ on FTO in the electrolyte solvent have been also studied with electrochemical impedance spectroscopy at different applied voltages as a powerful method to investigate the interface of the perovskite/electrolyte and identify the chemical changes at different electrode potentials and under illumination. The analysis of the impedance and the capacitance as well as exploring the response of the bulk and the interface of the perovskite provides us with important information about its properties and behavior in the solution that can advance the development of these two perovskite materials. For example, electrochemical impedance spectroscopy measurements under illumination suggest that $CsPbBr_3$ exhibits a lower charge transfer resistance underlining its potential for photocatalytic applications. However, the instability of lead halide perovskite films in most solvents still remains a challenge. Future work should focus on stabilizing the interface to minimize interfacial recombination, which as shown in this work, can be studied using electrochemical impedance spectroscopy.

BIBLIOGRAPHIE

Abdy, H., Heydari, Z., Aletayeb, A., Kolahdouz, M. et Asl-Soleimani, E. (2021, 2021/05/01). Electrodeposition, solvent engineering, and two-step solution deposition of the perovskite films: morphological and structural study. *Journal of Materials Science: Materials in Electronics*, *32*(10), 12991-12999. doi: 10.1007/s10854-020-03609-y

Bard, A. J. (1980). Photoelectrochemistry. *Science*, *207*(4427), 139-144. doi: doi:10.1126/science.207.4427.139

Cardenas-Morcoso, D., Gualdrón-Reyes, A. F., Ferreira Vitoreti, A. B., García-Tecedor, M., Yoon, S. J., Solis de la Fuente, M., . . . Gimenez, S. (2019, 2019/02/07). Photocatalytic and Photoelectrochemical Degradation of Organic Compounds with All-Inorganic Metal Halide Perovskite Quantum Dots. *The Journal of Physical Chemistry Letters*, *10*(3), 630-636. doi: 10.1021/acs.jpclett.8b03849

Chen, H., Wei, Z., Zheng, X. et Yang, S. (2015). A scalable electrodeposition route to the low-cost, versatile and controllable fabrication of perovskite solar cells. *Nano Energy*, *15*, 216-226. doi: 10.1016/j.nanoen.2015.04.025

Chong, M. N., Jin, B., Chow, C. W. et Saint, C. (2010, May). Recent developments in photocatalytic water treatment technology: a review. *Water Res*, *44*(10), 2997-3027. doi: 10.1016/j.watres.2010.02.039

Dandia, A., Saini, P., Sharma, R. et Parewa, V. (2020, 2020/06/01/). Visible light driven perovskite-based photocatalysts: A new candidate for green organic synthesis by photochemical protocol. *Current Research in Green and Sustainable Chemistry*, *3*, 100031. doi: https://doi.org/10.1016/j.crgsc.2020.100031

Elgrishi, N., Rountree, K. J., McCarthy, B. D., Rountree, E. S., Eisenhart, T. T. et Dempsey, J. L. (2018, 2018/02/13). A Practical Beginner's Guide to Cyclic Voltammetry. *Journal of Chemical Education*, *95*(2), 197-206. doi: 10.1021/acs.jchemed.7b00361

Gamburg, Y. et Zangari, G. (2011, 01/01). Theory and Practice of Metal Electrodeposition. doi: 10.1007/978-1-4419-9669-5

Georgi Popov, † Miika Mattinen,† Marianna L. Kemell,† Mikko Ritala,† and Markku Leskelä. (2015). Scalable route to fabrication of $CH_3NH_3PbI_3$ perovskite thin films by electrodeposition and vapor conversion

Guerrero, A., Bisquert, J. et Garcia-Belmonte, G. (2021, 2021/12/08). Impedance Spectroscopy of Metal Halide Perovskite Solar Cells from the Perspective of Equivalent Circuits. *Chemical Reviews*, *121*(23), 14430-14484. doi: 10.1021/acs.chemrev.1c00214

Herz, L. M. (2017, 2017/07/14). Charge-Carrier Mobilities in Metal Halide Perovskites: Fundamental Mechanisms and Limits. *ACS Energy Letters*, *2*(7), 1539-1548. doi: 10.1021/acsenergylett.7b00276

Holder, C. F. et Schaak, R. E. (2019, 2019/07/23). Tutorial on Powder X-ray Diffraction for Characterizing Nanoscale Materials. *ACS Nano*, *13*(7), 7359-7365. doi: 10.1021/acsnano.9b05157

Hsu, H.-Y., Ji, L., Ahn, H. S., Zhao, J., Yu, E. T. et Bard, A. J. (2015, 2015/11/25). A Liquid Junction Photoelectrochemical Solar Cell Based on p-Type $MeNH_3PbI_3$ Perovskite with 1.05 V Open-Circuit Photovoltage. *Journal of the American Chemical Society*, *137*(46), 14758-14764. doi: 10.1021/jacs.5b09758

Huang, H., Pradhan, B., Hofkens, J., Roeffaers, M. B. J. et Steele, J. A. (2020, 2020/04/10). Solar-Driven Metal Halide Perovskite tunable: Design, Stability, and Performance. *ACS Energy Letters*, *5*(4), 1107-1123. doi: 10.1021/acsenergylett.0c00058

Itagaki, M., Suzuki, S., Shitanda, I. et Watanabe, K. (2007). Electrochemical Impedance and Complex Capacitance to Interpret Electrochemical Capacitor. *Electrochemistry*, *75*(8), 649-655. doi: 10.5796/electrochemistry.75.649

Jaeyoung Lee a, Hamilton Varela a, Sunghyun Uhm b, Yongsug Tak b. (2000). Electrodeposition of PbO onto Au and Ti substrates. *Electrochemistry Communications* 646–665.

Klotz, D., Tumen-Ulzii, G., Qin, C., Matsushima, T. et Adachi, C. (2019). Detecting and identifying reversible changes in perovskite solar cells by electrochemical impedance spectroscopy. *RSC Advances*, *9*(57), 33436-33445. doi: 10.1039/C9RA07048F

Koza, J. A., Hill, J. C., Demster, A. C. et Switzer, J. A. (2016, 2016/01/12). Epitaxial Electrodeposition of Methylammonium Lead Iodide Perovskites. *Chemistry of Materials*, *28*(1), 399-405. doi: 10.1021/acs.chemmater.5b04524

Kumar, A., Kumar, A. et Krishnan, V. (2020, 2020/09/04). Perovskite Oxide Based Materials for Energy and Environment-Oriented Photocatalysis. *ACS Catalysis*, *10*(17), 10253-10315. doi: 10.1021/acscatal.0c02947

Kumar, S., Regue, M., Isaacs, M. A., Freeman, E. et Eslava, S. (2020, 2020/05/26). All-Inorganic $CsPbBr_3$ Nanocrystals: Gram-Scale Mechanochemical Synthesis and Selective Photocatalytic CO_2 Reduction to Methane. *ACS Applied Energy Materials*, *3*(5), 4509-4522. doi: 10.1021/acsaem.0c00195

Lv, P., Zhang, P., Chen, Z., Dong, S., Liu, M., Ma, J., . . . Li, S. (2020, 2020/09/01/). The preparation of all-inorganic $CsPbI_{2-x}Br_{1+x}$ perovskite solar cells based on electrodeposited PbO_2 film. *Solar Energy*, *207*, 618-625. doi: https://doi.org/10.1016/j.solener.2020.07.020

Mayer, M. T. (2017, 2017/04/01/). Photovoltage at semiconductor–electrolyte junctions. *Current Opinion in Electrochemistry*, *2*(1), 104-110. doi: https://doi.org/10.1016/j.coelec.2017.03.006

Peter, L. M. (2016). CHAPTER 1. Photoelectrochemistry: From Basic Principles to Photocatalysis. Dans *Photocatalysis* (p. 1-28).

Poli, I., Hintermair, U., Regue, M., Kumar, S., Sackville, E. V., Baker, J., . . . Cameron, P. J. (2019, 2019/05/08). Graphite-protected $CsPbBr_3$ perovskite photoanodes functionalised with water oxidation catalyst for oxygen evolution in water. *Nature Communications*, *10*(1), 2097. doi: 10.1038/s41467-019-10124-0

Popov, G., Mattinen, M., Kemell, M. L., Ritala, M. et Leskela, M. (2016, Dec 31). Scalable Route to the Fabrication of $CH_3NH_3PbI_3$ Perovskite Thin Films by Electrodeposition and Vapor Conversion. *ACS Omega*, *1*(6), 1296-1306. doi: 10.1021/acsomega.6b00351

Ranabhat, K., Patrikeev, L., Revina, A., Andrianov, K., Lapshinsky, V. et Sofronova, E. (2016, 01/01). An introduction to solar cell technology. *14*, 481-491. doi: 10.5937/jaes14-10879

Rühle, S. (2016, 2016/06/01/). Tabulated values of the Shockley–Queisser limit for single junction solar cells. *Solar Energy*, *130*, 139-147. doi: https://doi.org/10.1016/j.solener.2016.02.015

Samu, G. F., Scheidt, R. A., Kamat, P. V. et Janáky, C. (2018, 2018/02/13). Electrochemistry and Spectroelectrochemistry of Lead Halide Perovskite Films: Materials Science Aspects and Boundary Conditions. *Chemistry of Materials*, *30*(3), 561-569. doi: 10.1021/acs.chemmater.7b04321

Samu, G. F., Scheidt, R. A., Zaiats, G., Kamat, P. V. et Janáky, C. (2018, 2018/07/10). Electrodeposition of Hole-Transport Layer on Methylammonium Lead Iodide Film: A Strategy To Assemble Perovskite Solar Cells. *Chemistry of Materials*, *30*(13), 4202-4206. doi: 10.1021/acs.chemmater.8b01521

Singh, S., Chen, H., Shahrokhi, S., Wang, L. P., Lin, C.-H., Hu, L., . . . Wu, T. (2020, 2020/05/08). Hybrid Organic–Inorganic Materials and Composites for Photoelectrochemical Water Splitting. *ACS Energy Letters*, *5*(5), 1487-1497. doi: 10.1021/acsenergylett.0c00327

Tan, M. X., Laibinis, P. E., Nguyen, S. T., Kesselman, J. M., Stanton, C. E. et Lewis, N. S. (1994). Principles and Applications of Semiconductor Photoelectrochemistry. Dans *Progress in Inorganic Chemistry* (p. 21-144).

Tonui, P., Oseni, S. O., Sharma, G., Yan, Q. et Tessema Mola, G. (2018). Perovskites photovoltaic solar cells: An overview of current status. *Renewable and Sustainable Energy Reviews*, *91*, 1025-1044. doi: 10.1016/j.rser.2018.04.069

Wang, K., Lu, H., Zhu, X., Lin, Y., Beard, M. C., Yan, Y. et Chen, X. (2020, 2020/02/14). Ultrafast Reaction Mechanisms in Perovskite Based Photocatalytic C–C Coupling. *ACS Energy Letters*, *5*(2), 566-571. doi: 10.1021/acsenergylett.9b02714

Wang, W., Tadé, M. O. et Shao, Z. (2015). Research progress of perovskite materials in photocatalysis- and photovoltaics-related energy conversion and environmental treatment. *Chemical Society Reviews*, *44*(15), 5371-5408. doi: 10.1039/C5CS00113G

Zangari, G. (2018). Fundamentals of Electrodeposition. 141-160.

Zhang, D., Eaton, S. W., Yu, Y., Dou, L. et Yang, P. (2015, Jul 29). Solution-Phase Synthesis of Cesium Lead Halide Perovskite Nanowires. *J Am Chem Soc*, *137*(29), 9230-9233. doi: 10.1021/jacs.5b05404

Zhou, Y. et Zhao, Y. (2019). Chemical stability and instability of inorganic halide perovskites. *Energy & Environmental Science*, *12*(5), 1495-1511. doi: 10.1039/C8EE03559H